J. Fluid Mech. (2007), *vol.* 593, *pp.* 359–383.
doi:10.1017/S0022112007008816 Printed in the United Kingdom

The origin of the stationary frontal wave packet spontaneously generated in rotating stratified vortex dipoles

ÁLVARO VIÚDEZ

Institut de Ciències del Mar, CSIC, 08003 Barcelona, Spain

(Received 14 May 2007 and in revised form 28 August 2007)

The origin of the stationary frontal wave packet spontaneously generated in rotating and stably stratified vortex dipoles is investigated through high-resolution three-dimensional numerical simulations of non-hydrostatic volume-preserving flow under the f-plane and Boussinesq approximations. The wave packet is rendered better at mid-depths using ageostrophic quantities like the vertical velocity or the vertical shear of the ageostrophic vertical vorticity. The analysis of the origin of vertical velocity anomalies in shallow layers using the generalized omega-equation reveals that these anomalies are related to the material rate of change of the ageostrophic differential vorticity, which in shallow layers are themselves related to the large-scale ageostrophic flow along the dipole axis, and in particular, to the advective acceleration. It is found that on the anticyclonic side of the dipole axis the combined effect of the speed and centripetal accelerations causes an anticyclonic rotation of the horizontal ageostrophic vorticity vector in a time scale of about one inertial period. These facts support the hypothesis that the origin of the stationary and spontaneously generated frontal wave packet at mid-depths is the large acceleration of the fluid particles as they move along the anticyclonic side of the dipole axis in shallow layers.

1. Introduction

Inertia–gravity waves (IGWs) often develop in rotating stratified fluids such as the Earth's atmosphere and oceans (e.g. Miropol'sky 2001; Nappo 2002). The origin of these IGWs is usually external to the fluid itself. Some well-known examples are, in the case of oceanic IGWs, the forcing due to fluctuations of atmospheric pressure, changes in wind stress, and buoyancy flow fluctuations at the ocean surface. At the ocean floor and in the atmospheric boundary layer terrain-generated IGWs can develop in the form of lee waves and mountain waves. Besides this external wave generation, spontaneous generation of IGWs, that is without intervention of causes external to the otherwise balanced ocean and atmosphere interior flow, is also possible. This spontaneous IGW emission has been numerically simulated in barotropic unstable flows in rotating shallow water (Ford 1994) as well as numerically assessed in rotating two-layer shear flows (Williams, Read & Haine 2003). In the atmosphere spiral bands in tropical cyclones have been interpreted as a manifestation of spontaneous IGW generation (Chow, Chan & Lau 2002), and gravity wave generation found during the evolution of mesoscale convective cloud clusters (Lane, Reeder & Clark 2001), tropical cyclones (Pfister *et al.* 1993), frontogenesis (Griffiths & Reeder 1996; Reeder & Griffiths 1996; Snyder, Skamarock & Rotunno 1993), geostrophic adjustment (Fritts & Luo 1992; Luo & Fritts 1993), and baroclinic instability (O'Sullivan & Dunkerton

1995). Experimental evidence of spontaneous IGW generation has been reported from laboratory experiments in rotating two-layer flows (Williams, Haine & Read 2005) as well as from observations in the atmosphere (Bosart, Bracken & Seimon 1998; Plougonven, Teitelbaum & Zeitlin 2003, Lane *et al.* 2004). Spontaneous generation of IGWs has been also numerically simulated using three-dimensional primitive equation models of baroclinic waves in the atmosphere (O'Sullivan & Dunkerton 1995; Zhang 2004). Though the Rossby number $\mathscr{R}$ was larger than unity in some of the vortical flows exciting IGWs (Ford 1994; Ford, McIntyre & Norton 2000; Saujani & Shepherd 2002), there is increasingly persuasive evidence that spontaneous generation of IGWs will occur, as long as these are allowed by the dynamical equations used, even for flows initiated from perfectly well-balanced conditions (Lorenz & Krishnamurthy 1987; Farge & Sadourny 1989; Yuan & Hamilton 1994; Yavneh & McWilliams 1994; McWilliams & Yavneh 1998; Vanneste & Yavneh 2004).

Using a precise method for decomposing the flow into its balanced and unbalanced components Viúdez & Dritschel (2004) have found that small-amplitude IGWs are spontaneously generated, from rotating static and inertially stable unsteady baroclinic balanced flows ($\mathscr{R} < 1$ and Froude number $\mathscr{F} < 1$), in the form of three-dimensional wave packets. These wave packets propagate away from the wave sources and cause spiral wave patterns in the far field of the same sense of spiralling, cyclonic or anticyclonic, as the moving IGW sources (Viúdez 2006). The precise physical mechanism that causes the emission of these wave packets remains unclear, to a large extent because the balanced flow is unsteady and the IGW emission is discrete. There are however several geophysical coherent three-dimensional vortex structures, the simplest being the baroclinic dipole, where the spontaneous IGW emission is continuous and the wave packet remains steady in the reference frame relative to the moving dipole (Viúdez 2006, 2007). These characteristics make the *frontal* wave packet, referred to in this way because it develops at the front of the dipolar structures, an exceptional case to investigate the physical mechanism responsible for spontaneous IGW generation. The existence of the frontal wave packet has also been recently and independently described using numerical techniques very different to the ones used here (Snyder *et al.* 2007). This paper describes the results of the search for a mechanistic explanation of the frontal wave packet using high-resolution three-dimensional numerical simulations of non-hydrostatic volume-preserving flow under the f-plane and Boussinesq approximations. The theoretical background, numerical model and initial conditions are explained in § 2.

There are at least three key features important for an understanding of the frontal wave packet. The first feature is the initial wave packet generation forced by the vortical flow or, in other words, the 'first push' that triggers the oscillatory motion of the fluid particles. It is suggested here that in the frontal wave packet this initial generation is caused mainly by the large-scale dipolar flow in shallow layers along the anticyclonic side of the dipole axis. When the fluid particles move along the dipole axis they initially accelerate as they enter from the rear, and subsequently decelerate as they reach the frontal part. The time scale in which this perturbation takes place is estimated as the ratio $\mathscr{L}/\mathscr{U}$ between the horizontal dipole scale $\mathscr{L}$ and the typical fluid velocity along the dipole axis $\mathscr{U}$ relative to the moving dipole reference frame. If this time scale has an order of magnitude similar to the inertial period $2\pi/f$, where f is the Coriolis frequency, then this perturbation triggers the first quasi-inertial oscillation of the fluid particles. The main objective of this paper is to make this idea precise and show that this is indeed the case in the frontal wave packet. A first difficulty is that, besides the large-scale structure of the initial wave perturbation,

other large-scale structures, related to quasi-geostrophic (QG) balanced mesoscale dynamics and not related to the wave generation, coexist in the dipolar flow. Thus, it is necessary to distinguish the different origins of these similar large-scale structures. As is typical in rotating stratified flows, the amplitude of the horizontal velocity perturbation is very small relative to the amplitude of the vortical horizontal velocity, which is largely geostrophic or cyclostrophic in the dipole. Hence it is convenient to analyse the wave perturbation in terms of smaller ageostrophic quantities, such as the vertical velocity perturbation, which may become of the same order of magnitude as the balanced vertical velocity.

The vertical velocity field is examined at different depths (§ 3) and it is found that, while the frontal wave packet clearly develops at mid-depths, some large-scale patterns in the vertical velocity develop in shallow layers along the dipole axis. These vertical velocity patterns seem to be the initial generation of the frontal wave, which is first excited with small wavenumbers. The origin of these large-scale perturbations in the vertical velocity is then explored using the generalized omega-equation (§ 4), which is interpreted as an equation for the material rate of change of the vertical shear of the ageostrophic vertical vorticity (ζ_z'). It is found that these velocity perturbations in shallow layers are related to the advection of ζ_z', and are therefore not QG contributions. This strongly supports their wave-like nature since IGWs are not permissible in the QG dynamics.

The second key feature in understanding the frontal wave packet is the process by which motion is transferred from the large spatial scales of the initial wave perturbation to the short spatial scales typical of the unbalanced wave flow. In the frontal wave packet this process is simply particle advection by a decelerating flow. When the fluid particle, which is experiencing small-amplitude oscillations, continues its background deceleration as it leaves the dipole centre, its horizontal wavenumber decreases as $\sim u^{-1}$ (where u is the balanced horizontal fluid velocity relative to the moving dipole) due to the decreasing horizontal particle displacement per oscillation period. This kinematic effect is similar to that of a pendulum oscillating with constant frequency along the y-axis and being simultaneously transported with velocity u along the x-axis. Kinematically, as u slowly decreases, the wavenumber in the x-direction (k) must increase since the x-displacement per unit time (or per oscillating period) decreases. It is in this regime where the frontal wave packet approximately satisfies IGW solutions in the background flow. In § 5 the ageostrophic shear vorticity is analysed and related to the ageostrophic motion, and in particular related to the flow acceleration along the dipole axis at shallow depths. The evolution of the frontal wave packet along the dipole axis at mid-depths and its intrusion inside the vortices is described from time series of the total vertical velocity (§ 6).

Finally, a third key feature of the frontal wave packet is the wave amplitude damping. Obviously the wavenumber cannot increase indefinitely. Numerically a finite limit is reached when the wavenumber becomes similar to the maximum wavenumber allowed by the model spatial discretization. At this time the wave amplitude is damped by numerical diffusion as a way to prevent grid-size numerical instability. Wave breaking and turbulent diffusion, and ultimately molecular diffusion, would in nature damp the frontal wave packet at very high wavenumbers.

2. Theoretical background, numerical model and initial conditions

2.1. *Theoretical background and numerical model*

The three-dimensional baroclinic stably stratified volume-preserving non-hydrostatic flow, under the f-plane and Boussinesq approximations, is simulated using a triply

periodic numerical model (Dritschel & Viúdez 2003) initialized with the potential vorticity (PV) initialization approach (Viúdez & Dritschel 2003). The theoretical basis of the numerical model is explained in detail in the references above and succinctly here in the Appendix, and only a brief summary is given next to introduce the required symbol definitions and mathematical expressions. We analyse results from numerical simulations with 128^3 (hereafter case 1, C1) and 512^3 (hereafter case 2, C2) grid points, having 128 and 512 isopycnals, respectively. The PV is represented by contours on isopycnal surfaces. The domain has a vertical extent $L_Z = 2\pi$ (which defines the unit of length) and horizontal extents $L_X = L_Y = cL_Z$, where $c \equiv 10$ is the ratio of the background Brunt–Väisälä frequency to the Coriolis frequency: $c \equiv \epsilon^{-1} \equiv N/f$. The mean buoyancy period ($T_{bp} \equiv 2\pi/N$) is set as the unit of time (thus $N \equiv 2\pi$). One inertial period ($T_{ip} \equiv 2\pi/f$) equals $10\,T_{bp}$.

The vertical displacement of isopycnals is $\mathscr{D}(\boldsymbol{x}, t) \equiv z - d(\boldsymbol{x}, t)$, where $d(\boldsymbol{x}, t) \equiv (\rho(\boldsymbol{x}, t) - \rho_0)/\varrho_Z$ is the depth of an isopycnal located at $\boldsymbol{x}$ at time t in the reference density configuration defined by $\rho_0 + \varrho_Z z$, where ρ is the mass density, and $\rho_0 > 0$ and $\varrho_Z < 0$ are constants which do not need to be specified in the Boussinesq approximation. The squared mean Brunt–Väisälä frequency $N^2 \equiv -\alpha_0\, g\, \varrho_Z$, where $\alpha_0 \equiv 1/\rho_0$ and g is the acceleration due to gravity. Static instability occurs when the stratification number $\mathscr{D}_z \equiv \partial\mathscr{D}/\partial z > 1$. The Rossby number $\mathscr{R} \equiv \zeta/f$, and the Froude number $\mathscr{F} \equiv \omega_h/\mathscr{N}$, where $\omega_h \equiv |\boldsymbol{\omega}_h|$ and ζ are the horizontal and vertical components of the relative vorticity $\boldsymbol{\omega} = \boldsymbol{\omega}_h + \zeta \boldsymbol{k}$, respectively, and $\mathscr{N}^2 \equiv -\alpha_0\, g\, \partial\rho/\partial z = N^2(1 - \mathscr{D}_z)$ is the squared total Brunt-Väisälä frequency. Subscript h denotes the horizontal component. The state variables are the components of the vector potential $\boldsymbol{\varphi} \equiv (\varphi, \psi, \phi)$ from which both the three-dimensional velocity $\boldsymbol{u} = (u, v, w)$ and isopycnal vertical displacement $\mathscr{D}$ are obtained:

$$\boldsymbol{u} = -f\nabla \times \boldsymbol{\varphi}\,, \quad \mathscr{D} = -\epsilon^2 \nabla \cdot \boldsymbol{\varphi}. \tag{2.1}$$

Let $\tilde{\chi} \equiv \chi/f$ for any quantity χ. The numerical model integrates three equations. Two are for the rate of change of the dimensionless horizontal ageostrophic vorticity

$$\begin{aligned} \mathscr{A}_h &= (\mathscr{A}, \mathscr{B}) \equiv \tilde{\boldsymbol{\omega}}_h - c^2 \nabla_h \mathscr{D} \equiv \tilde{\boldsymbol{\omega}}_h - \tilde{\boldsymbol{\omega}}_h^g \equiv \tilde{\boldsymbol{\omega}}_h' \\ &= [-\nabla \times (\nabla \times \boldsymbol{\varphi}) + \nabla(\nabla \cdot \boldsymbol{\varphi})]_h = \nabla^2 \boldsymbol{\varphi}_h = (\nabla^2\varphi, \nabla^2\psi)\,, \end{aligned} \tag{2.2}$$

where $\boldsymbol{\omega}_h^g$ is the horizontal geostrophic vorticity. The material rate of change of $\mathscr{A}_h$ (see (A 19)) is

$$\frac{\mathrm{d}\mathscr{A}_h}{\mathrm{d}t} = -f\boldsymbol{k} \times \mathscr{A}_h + (1 - c^2)\nabla_h w + \tilde{\boldsymbol{\omega}} \cdot \nabla \boldsymbol{u}_h + c^2 \nabla_h \boldsymbol{u} \cdot \nabla \mathscr{D}. \tag{2.3}$$

The above equation is numerically integrated using an explicit leap-frog scheme, together with a weak Robert–Asselin time filter to avoid the decoupling between even and odd time levels. Spatial derivatives are carried out in the spectral space. A biharmonic hyperdiffusion term, producing a small damping rate (e folding) per inertial period at the highest wavenumber equal to $e_f = 50$ (C1) and $e_f = 200$ (C2) is added to (2.3) to avoid the generation of grid-size noise.

The third equation is the explicit material conservation of the PV anomaly ϖ by contour advection on isopycnals ($\mathrm{d}\varpi/\mathrm{d}t = 0$), where

$$\varpi \equiv \Pi - 1 \equiv (\tilde{\boldsymbol{\omega}} + \boldsymbol{k}) \cdot (\boldsymbol{k} - \nabla\mathscr{D}) - 1 = \tilde{\zeta} - \mathscr{D}_z - \tilde{\boldsymbol{\omega}} \cdot \nabla\mathscr{D}, \tag{2.4}$$

and $\Pi \equiv (\tilde{\boldsymbol{\omega}} + \boldsymbol{k}) \cdot \nabla d$ is the dimensionless total PV. The locations of the PV contours are numerically integrated in time using a standard third-order three-time-level Adams–Bashforth scheme. The horizontal potentials $\boldsymbol{\varphi}_h = (\varphi, \psi)$ are recovered from the inversion, in the spectral space, of $\mathscr{A}_h = \nabla^2 \boldsymbol{\varphi}_h$, while the vertical potential ϕ is

obtained from the inversion of the definition of ϖ (2.4) in terms of the potentials, $\varpi = \varpi(\varphi, \psi, \phi)$.

The dimensionless horizontal ageostrophic vorticity $\mathscr{A}_h$ is related to the dimensionless horizontal ageostrophic pseudovorticity $\tilde{\boldsymbol{\zeta}}'_h \equiv [\nabla \times \boldsymbol{u}'_h]_h / f = (-\partial v/\partial z, \partial u/\partial z)/f$, that is the horizontal vorticity of the horizontal ageostrophic velocity $\boldsymbol{u}'_h$, also called the thermal-wind imbalance vector, by

$$\mathscr{A}_h = \tilde{\boldsymbol{\zeta}}'_h - \boldsymbol{k} \times \nabla_h \tilde{w}. \tag{2.5}$$

Two quantities relevant in the analysis of the IGWs are the vertical shear of the ageostrophic vertical vorticity $\zeta'_z \equiv \partial \zeta'/\partial z$, where $\zeta' \equiv \zeta - \zeta^g$ is the ageostrophic vertical vorticity, and the Laplacian of w, $\nabla^2 w$. These two ageostrophic quantities (divided by f) are, respectively, the (negative) divergence and curl of $\mathscr{A}_h$:

$$\tilde{\zeta}'_z = -\nabla_h \cdot \mathscr{A}_h, \quad \nabla^2 \tilde{w} = -\boldsymbol{k} \cdot \nabla_h \times \mathscr{A}_h, \tag{2.6a,b}$$

and are therefore independent of the vertical potential ϕ.

2.2. *The initial conditions*

The baroclinic dipoles are initiated as two ellipsoids of oppositely signed ϖ. The number of initial PV contours in the middle isopycnal (isopycnal index $i_l = 65$ and $i_l = 257$ in the C1 and C2 simulations, respectively) of each vortex is $n_c = 20$ (C1) and $n_c = 60$ (C2). The PV anomaly ϖ varies from $\varpi \cong 0$ (outermost surface) to extrema $\varpi^{\pm} = \pm 0.85$ (C1), and $(\varpi^-, \varpi^+) = (-0.8, 1.8)$ (C2), in the vortex cores. The ϖ jump is fixed for the contours in every vortex $\delta\varpi^{\pm} = |\varpi^{\pm}|/n_c$. Initially the outermost ϖ ellipsoidal layer has horizontal major and minor semi-axes $(a_X^{\pm}, a_Y^{\pm}) = (1.4, 1.2)c$, and vertical semi-axes $(a_Z^+, a_Z^-) = (1.2, 0.52)$ (C1). The same values were used in C2 except that the initial vertical extents of the vortices were equal, $a_Z^{\pm} = 1.2$. Further details on the PV configuration of the three-dimensional ellipsoids are given in Viúdez & Dritschel (2003). The initial distance between vortex centres is $2a_Y^{\pm} + 0.01c$. The ϖ ellipsoids are initially defined on the isopycnal space (or, equivalently, in the physical space with flat isopycnals).

During the initialization period t_I of the PV initialization method (here we set $t_I = 5\,T_{ip}$) the PV anomaly grows smoothly for every fluid particle, i.e. in a Lagrangian way, so that both $\boldsymbol{u}$ and $\mathscr{D}$ grow smoothly as well. Therefore, during the initialization period ($0 \leqslant t \leqslant t_I$), and due to the thermal-wind relation, the isopycnals in the anticyclone stretch and those in the cyclone shrink, in such a way that at $t = t_I$ both vortices have similar vertical extents in C1. In C2 the vertical extent of the anticyclone in larger than that of the cyclone. This has little importance for the development of the frontal wave however, which is a robust phenomenon in dipolar flows with $|\mathscr{R}| \lesssim 1$. The extreme Rossby numbers $(\mathscr{R}_{\min}, \mathscr{R}_{\max})$ were $(-0.73, 0.48)$ and $(-0.82, 0.81)$ in C1 and C2, respectively, while the maximum Froude number $\mathscr{F}_{\max}(t) \subset [0.43, 0.48]$ for $t = [5, 50]\,T_{ip}$ (C1, with time average and standard deviation $\langle \mathscr{F}_{\max} \rangle = 0.45 \pm 0.01$), and $\mathscr{F}_{\max}(t) \subset [0.41, 0.75]$, for $t = [5, 17]\,T_{ip}$ (C2, with $\langle \mathscr{F}_{\max} \rangle = 0.56 \pm 0.08$). As we describe below, the frontal wave packet is generated in both cases.

3. The frontal wave packet at different depths

In Viúdez (2007) the frontal wave packet was extracted from the balanced dipolar flow using the optimal PV balance approach. An analysis of the extracted unbalanced flow revealed that the wave packet (i) is stationary relative to the translating dipole, (ii) has wavenumbers that depend on the horizontal and vertical derivatives of the

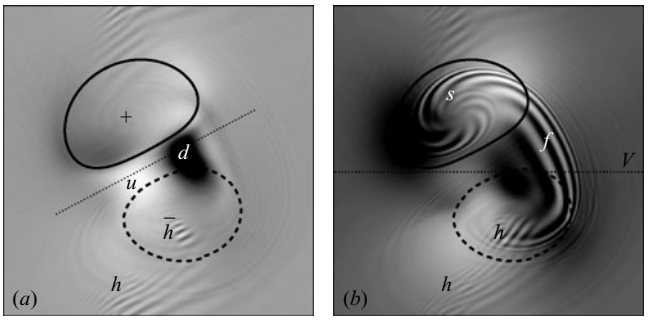

FIGURE 1. Horizontal distribution of vertical velocity $w(x, y)$ at (*a*) $z \simeq -0.2$ ($i_Z = 240$, $w \in [-6.9, 5.1] \times 10^{-3}$), and (*b*) $z \simeq -0.9$ ($i_Z = 180$, $w \in [-5.2, 8.3] \times 10^{-3}$), for C2 ($t = 17\, T_{ip}$). The PV contours $\varpi = \pm 0.5$, the along-dipole axis, and the vertical section V are included for reference. The labels denote: cyclone (+), anticyclone (−), upwelling (*u*), downwelling (*d*), spiral wave (*s*), frontal wave (*f*), and heading waves (*h*).

background dipolar flow, and (iii) is generated somewhere in the upper layer ($z \lesssim 0$), predominantly on the anticyclonic side of the dipole, and afterwards propagates downward (until the stationary state is reached). Since the domain is triply periodic a second wave packet develops at $z \gtrsim 0$ and propagates upwards. The optimal PV balance (OPVB) approach provides, from a given three-dimensional PV field, a flow (namely, the OPVB vector potential $\boldsymbol{\varphi}_b$) having only those IGWs that have been spontaneously generated during the process of acquiring PV (during a time interval set equal to the initialization period $t_I = 5\, T_{ip}$). Therefore, the OPVB approach correctly extracted that part of the frontal wave packet (through the imbalance vector potential $\boldsymbol{\varphi}_i \equiv \boldsymbol{\varphi} - \boldsymbol{\varphi}_b$) located at the dipole head, away from the dipole centre, because the frontal wave is not spontaneously generated locally there in a short time period, i.e. shorter than t_I. However, if the first waves of the frontal wave are spontaneously generated in the upper layers of the dipole centre, then the OPVB approach only partially extracted the frontal wave packet: the first crests and troughs remained in the OPVB flow, since these early waves are unlikely to obey a dynamics separable from the dynamics of the total flow. This is not a weakness of the OPVB approach, which works very well after the wave emission has taken place, but it is due to the fact that, in this case, any hypothetical and potentially obtainable balanced state (in the sense of being free of waves) will not remain so for an infinitesimally small period of time. Once the IGWs propagate forward and downwards, arriving at the dipole head, they obey a separate dynamics, that is, the dynamics of IGWs in a background flow, and are therefore separable from the dipole balanced flow. Generally speaking, the initial spontaneous generation of waves is a process essentially dependent on the vortical flow and therefore seems to be inseparable. As a consequence, the initial stages of the frontal wave are identified better in the total vertical velocity $w \equiv -f\boldsymbol{k} \cdot \boldsymbol{\nabla} \times \boldsymbol{\varphi}$ than in the unbalanced vertical velocity $w_i \equiv -f\boldsymbol{k} \cdot \boldsymbol{\nabla} \times \boldsymbol{\varphi}_i$.

In the baroclinic dipole, as the fast fluid particles close to the surface layers enter through the rear part of the dipole axis, they first ascend ($w > 0$, upwelling), and subsequently descend ($w < 0$, downwelling) as they leave the dipole axis (labels *u* and *d*, respectively, in the horizontal and vertical distributions of w in figures 1*a* and 2). A second wave (crest and trough) of smaller amplitude is also observed at the dipole head in the shallow layer shown in figure 1(*a*). The main hypothesis of this work is that the frontal wave packet is generated in these upper layers by the accelerating flow, the initial waves of the frontal wave packet having a small wavenumber and

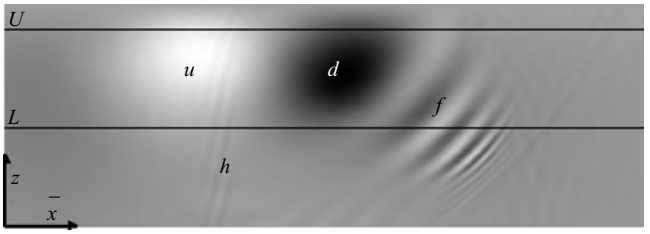

FIGURE 2. Vertical distribution of vertical velocity $w(y, z)$ crossing the frontal wave along the vertical section V (figure 1b) for C2 ($w \in [-9.8, 9.8] \times 10^{-3}$, $t = 17\,T_{ip}$). The labels denote: upwelling (u), downwelling (d), frontal wave (f), and heading wave (h). The upper (U, $z \simeq -0.2$, $i_Z = 240$) and lower (L, $z \simeq -0.9$, $i_Z = 180$) horizontal planes in figures 1(a) and 1(b), respectively, are included.

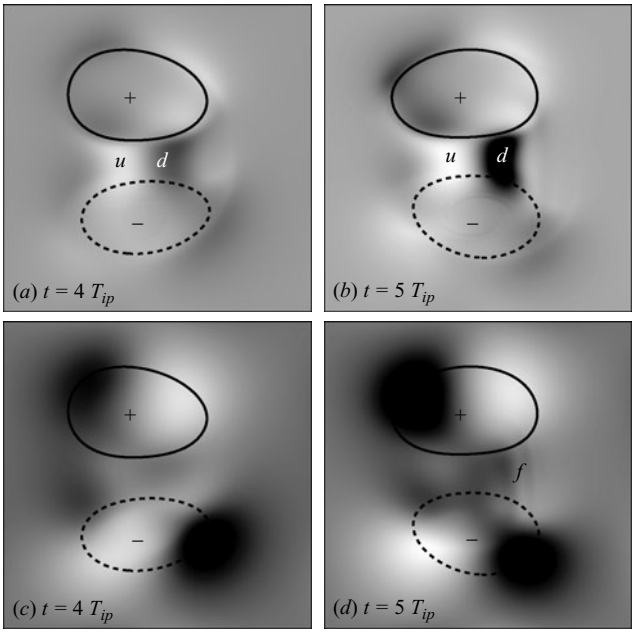

FIGURE 3. Horizontal distributions of $w(y, z)$ for C2 at depths (a, b) $z \simeq -0.2$ ($w \in [-4.4, 2.9] \times 10^{-3}$), and ($c, d$) $z \simeq -1.2$ ($w \in [-3.0, 3.6] \times 10^{-3}$), and times $t = 4\,T_{ip}$ and $t = 5\,T_{ip}$. The PV contours $\varpi = \pm 0.5$ at $z = 0$ are included. The labels denote: upwelling (u), downwelling (d), and frontal wave (f).

therefore a large-scale pattern (locations u and d in figures 1a and 2), and then propagates forward and downward, the wavenumber increasing as the horizontal velocity decreases, resulting in a frontal wave with a clear wave packet structure in deep layers (location f in figures 1b and 2). The initial velocity and density perturbations are subsequently transmitted to the fluid particles, rotating inside the vortices and temporarily located nearby the dipole axis, which start oscillating causing the spiral wave pattern (locations s in figure 1b) clearly visible in the cyclone. The time evolution of these spiral waves is described in more detail in § 6.

The early evolution of the wave packet is shown in terms of w at two different levels in figure 3. At $t = 4\,T_{ip}$, that is, $1\,T_{ip}$ before the initialization time is completed, the incipient u and d regions are already noticeable in shallow layers (figure 3a),

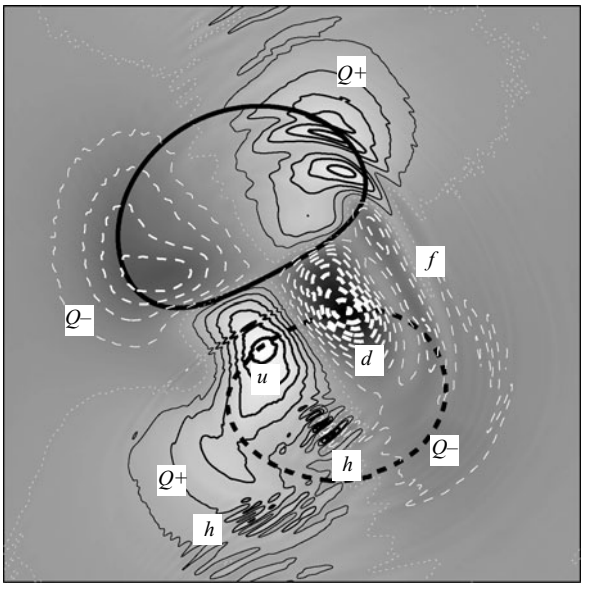

FIGURE 4. Horizontal distribution of vertical velocity $w(x, y)$ at $z \simeq -0.58$ for C2 ($i_Z = 210$, $w \in [-10, 6.6] \times 10^{-3}$, contour interval $\delta w = 10^{-3}$). The labels denote: upwelling (u), downwelling (d), frontal wave (f), heading waves (h), and the quadrupolar pattern of mesoscale vertical velocity ($Q\pm$). Horizontal extent $\delta x = \delta y = 2\pi c$.

while the frontal wave is absent in deep layers (figure 3*c*). At the end of the initialization time ($t = 5\,T_{ip}$) the u and d regions are already fully developed (figure 3*b*), while the frontal wave packet starts to have a very small amplitude in deep layers (figure 3*d*). Thus, if it is accepted that the upwelling and downwelling regions in shallow layers are the initial waves of the frontal wave packet, then the wave packet propagates, during the short time scale of a few inertial periods, from the upper to the lower layers. The subsequent development at $t \geqslant 5\,T_{ip}$ of the frontal wave in deep layers, and in particular the longer evolution of its spiral branches inside the vortices, is described in detail in § 6. Once fully developed, the frontal wave packet is stationary relative to the dipole reference frame, so it does not propagate in this frame.

In the anticyclone the spiral wave pattern is distorted by the spontaneous generation of heading waves. These waves (location h in figures 1*b* and 2) are generated by phase oscillations of the baroclinic vortices, or dipole heading, particularly in this case by the anticyclone. In this case the dipole heading has a periodicity of approximately $4\,T_{ip}$, which coincides with the periodicity of the discrete heading wave generation, as it is confirmed later in § 6 from time series of horizontal distributions of w. Two wave packets of heading waves, emitted at two different times and propagating southward, are clearly noticeable in figure 1(*b*). The dipole heading and the generation of propagating heading waves seem to be independent of the stationary frontal wave packet and will not be addressed further here.

Simultaneously with the spontaneous generation of wave motion, the fluid particles have the balanced vertical velocity typical of the mesoscale background dipolar flow, consisting of the quadrupolar pattern seen as four large-scale light and dark areas broadly located at the apices of the vortices in figure 1(*b*). This QG vertical velocity is also clearly noticeable, together with the wave motion, in the discrete w contours at mid depth in figure 4.

To investigate the hypothesis that the frontal wave packet is generated in the upper layers, where it has a large-scale pattern, by the background dipole flow acceleration, an analysis of the origin of this large-scale vertical velocity structure at the dipole centre is carried out in the next section using the generalized omega-equation (ω-equation). The objective is to show that these extreme w values (labelled u and d), although having a large spatial extent, do not have a QG origin, are therefore different from the other w extrema, and are mainly related to the material rate of change of the differential ageostrophic vertical vorticity $\tilde{\zeta}_z'$.

4. Analysis of the vertical velocity using the generalized ω-equation

The generalized ω-equation (Viúdez, Tintoré & Haney 1996) can be interpreted as an equation for the material rate of change of the differential ageostrophic vertical vorticity $\tilde{\zeta}_z'$ and consequently expressed as

$$\begin{aligned}\frac{\mathrm{d}\tilde{\zeta}_z'}{\mathrm{d}t} &= \frac{\partial\tilde{\zeta}_z'}{\partial t} + \boldsymbol{u}_h\cdot\nabla_h\tilde{\zeta}_z' + w\frac{\partial\tilde{\zeta}_z'}{\partial z}\\ &= -\nabla_h\cdot[2\boldsymbol{Q}_h + c^2(\mathscr{D}_z-1)\nabla_h w] + (\tilde{\zeta}+1)w_{zz} + \tilde{\boldsymbol{\zeta}}_{hz}'\cdot\nabla_h w - \tilde{\boldsymbol{\zeta}}_h'\cdot\nabla_h^2\boldsymbol{u}_h\\ &= -2\nabla_h\cdot\boldsymbol{Q}_h + \underbrace{c^2\nabla_h^2 w + w_{zz}}_{\mathscr{L}^q\{w\}}\\ &\quad \underbrace{-c^2\nabla_h\cdot(\mathscr{D}_z\nabla_h w)}_{T_3} + \underbrace{\tilde{\zeta}w_{zz} + \tilde{\boldsymbol{\zeta}}_{hz}'\cdot\nabla_h w}_{T_2} \underbrace{-\tilde{\boldsymbol{\zeta}}_h'\cdot\nabla_h^2\boldsymbol{u}_h}_{T_1},\end{aligned} \tag{4.1}$$

where the horizontal vector $\boldsymbol{Q}_h \equiv c^2\nabla_h\boldsymbol{u}_h\cdot\nabla_h\mathscr{D}$, and the subscript z denotes the partial derivative with respect to z. Using (2.6a) equation (4.1) can be interpreted as the horizontal divergence of (2.3). In the QG approximation, the horizontal velocity is replaced by its geostrophic approximation ($\boldsymbol{u}_h \to \boldsymbol{u}_h^g$), and assuming that for small Rossby numbers the flow is both inertially very stable ($|\tilde{\zeta}| \ll 1$) and statically very stable ($|\mathscr{D}_z| \ll 1$), the QG approximation of (4.1) is the $\boldsymbol{Q}$-vector QG ω-equation

$$\mathscr{L}^q\{w^q\} = 2\nabla_h\cdot\boldsymbol{Q}_h^g, \tag{4.2}$$

where $\boldsymbol{Q}_h^g \equiv c^2\nabla_h\boldsymbol{u}_h^g\cdot\nabla_h\mathscr{D}$ is the horizontal geostrophic $\boldsymbol{Q}$ vector, w^q is the QG vertical velocity, and the linear operator $\mathscr{L}^q \equiv c^2\nabla_h^2 + \partial_{zz}$ is the QG Laplacian operator. The material rate of change of $\tilde{\zeta}_z'$ is neglected. This linear equation is directly solved for w^q by inverting the operator $\mathscr{L}^q$ in spectral space.

The horizontal distribution of w^q at mid depth (figure 5a) displays the typical quadrupolar pattern of balanced vertical velocity in dipoles (Pallàs-Sanz & Viúdez 2007). These QG extrema are labelled with symbols $Q\pm$. The upwelling and downwelling regions on the dipole axis (labelled u and d, respectively, in figure 4) are missing in w^q, and are therefore not associated with the QG balanced dynamics.

Furthermore, these upwelling and downwelling motions are not fully explained by the non-QG forcing of the generalized $\boldsymbol{Q}$-vector. The solution of the truncated ω-equation

$$\mathscr{L}^q\{w^t\} = 2\nabla_h\cdot\boldsymbol{Q}_h, \tag{4.3}$$

which differs from (4.2) in that the forcing term includes now the divergence of the total vector $\boldsymbol{Q}_h \equiv c^2\nabla_h\boldsymbol{u}_h\cdot\nabla_h\mathscr{D}$ as in (4.1), is shown at mid depth in figure 5(b). The horizontal distribution of w^t broadly displays, with larger amplitudes, the large-scale quadrupolar pattern of w^q, but differs from w along the dipole axis where it

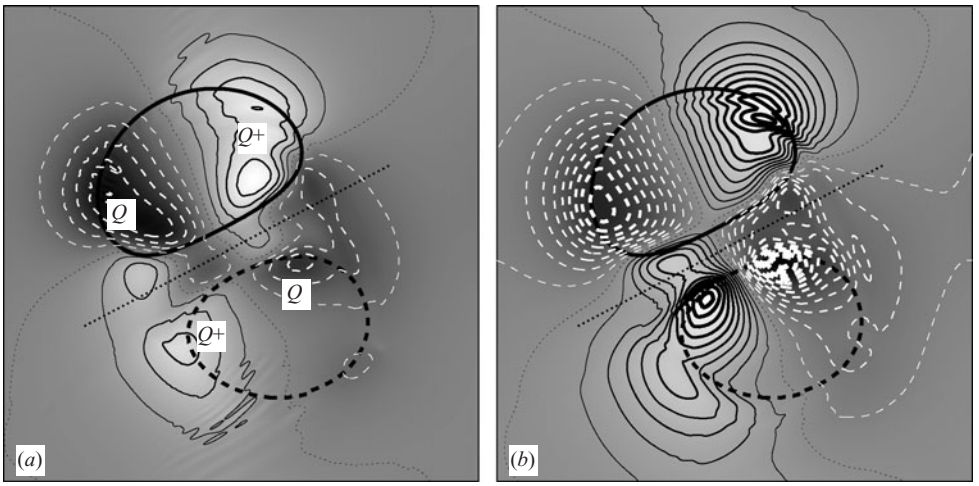

FIGURE 5. Horizontal distribution, for C2, of (*a*) the QG vertical velocity $w^q(x, y)$ ($w^q \in [-2.6, 2.4] \times 10^{-3}$, and (*b*) $w^t(x, y)$ ($w^t \in [-6.3, 5.2] \times 10^{-3}$), at $z \simeq -0.58$ ($i_Z = 210$, contour interval $\delta = 0.5 \times 10^{-3}$). The labels $Q\pm$ indicate the quadrupolar pattern of QG vertical velocity.

only partially reproduces the upwelling and downwelling motion of w (the contour interval in figure 5 is half that of figure 4).

We now analyse in detail C1 because the frontal wave packet also develops in this case, and the lower numerical resolution used avoids the generation of smaller scale waves, which do not significantly interfere with the frontal wave packet but may graphically mask the larger scale patterns of interest. At the same time the lower numerical resolution makes the analysis computationally easier that for C2. Note however that, owing to the different extreme Rossby numbers for C1 and C2, significant differences, especially in the vertical velocity, are expected between these cases. The total vertical velocity w at mid- and shallow depths (figure 6) displays the quadrupolar pattern of QG extrema similar to those for C2 at the external sides of the dipole (labelled as $Q\pm$) plus other QG extrema in the dipole interior (labelled as $q\pm$), which correspond to the QG vertical velocity w^q extrema shown in figure 7(*a*). The frontal wave packet is also clearly noticeable in w at mid depth (labelled f in figure 6*a*), while two non-QG regions of upwelling and downwelling (labelled u and d, respectively) occur at mid- and shallow depths on the dipole axis and inside the anticyclone. The magnitude of w in the regions u and d at a shallow depth (figure 6*b*) is larger than at mid depth (figure 6*a*), where the frontal wave, having shorter wavelength, is more noticeable however. This is in contrast to the QG extrema, which at mid depth are larger than at shallow depth, and supports the hypothesis that these u and d consecutive extrema are in fact related to the first wave of the frontal wave packet.

The origin of the u and d extrema is not related to the other forcing terms on the right-hand side of (4.1). The solution w^{ql} (superscript ql denotes Q-vector and Laplacian) of the truncated ω-equation

$$\mathscr{L}^q\{w^{ql}\} = 2\nabla_h \cdot \boldsymbol{Q}_h + \tilde{\boldsymbol{\xi}}'_h \cdot \nabla_h^2 \boldsymbol{u}_h, \tag{4.4}$$

which differs from (4.3) by the addition of the Laplacian forcing term $\tilde{\boldsymbol{\xi}}'_h \cdot \nabla_h^2 \boldsymbol{u}_h$ (term T_1 in (4.1)) is compared with w^q in figure 7(*b*). The solution w^{ql} has a pattern

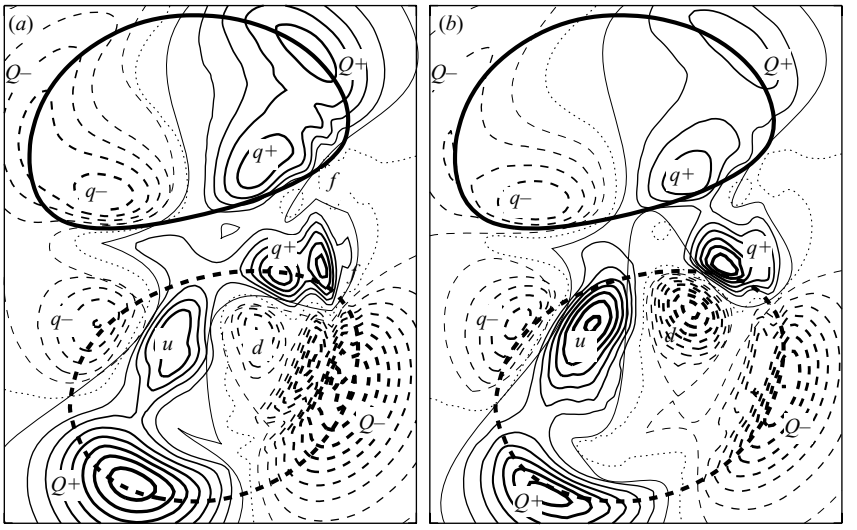

FIGURE 6. Horizontal distribution for C1 of $w(x, y)$ at (*a*) $z \simeq -0.49$ ($i_Z = 55$, $w \in [-1.9, 1.7] \times 10^{-3}$), and (*b*) $z \simeq -0.29$ ($i_Z = 59$, $w \in [-1.6, 1.6] \times 10^{-3}$). Contour interval $\delta w = 0.2 \times 10^{-3}$, $t = 9\,T_{ip}$, and horizontal extent $(\delta x, \delta y) = (3.9, 4.9)c$, with the aspect ratio preserved. The labels $Q\pm$ and $q\pm$ indicate the w extrema associated with QG vertical velocity. The frontal wave packet is also noticeable (labels *f*). The PV contours $\varpi = \pm 0.2$ are included for reference.

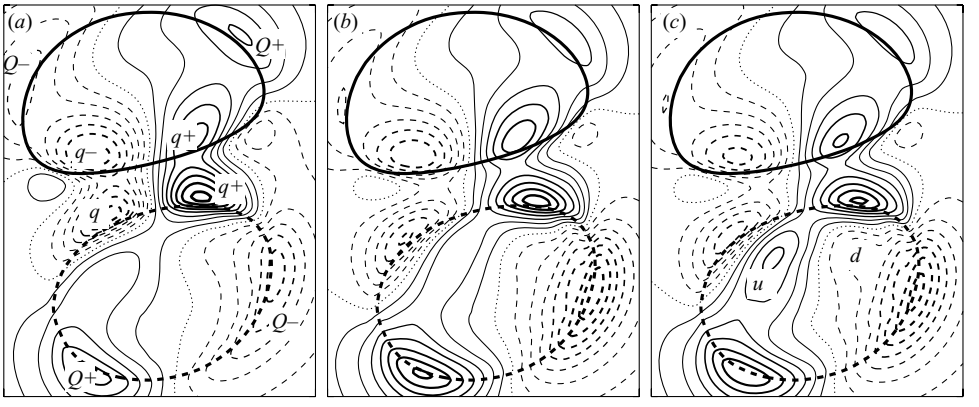

FIGURE 7. Horizontal distribution for C1 at $z \simeq -0.49$ ($i_Z = 59$) of (*a*) w^q ($w^q \in [-1.3, 1.7] \times 10^{-3}$); (*b*) w^{ql} ($w^{ql} \in [-1.5, 1.5] \times 10^{-3}$); and (*c*) w^v ($w^v \in [-1.5, 1.5] \times 10^{-3}$). Contour interval $\delta w = 0.2 \times 10^{-3}$ and horizontal extent $(\delta x, \delta y) = (3.9, 4.9)c$, with the aspect ratio preserved. The labels $Q\pm$ and $q\pm$ indicate the w extrema associated with the QG vertical velocity. The PV contours $\varpi = \pm 0.2$ are included for reference.

qualitatively similar to w^q (figure 7*a*), and is therefore also unable to reproduce the u and d vertical motion.

The next vertical velocity field w^v (superscript v denotes vertical velocity) that we consider is a solution of the reduced ω-equation

$$\mathscr{L}^q\{w^v\} = 2\nabla_h \cdot \boldsymbol{Q}_h + \tilde{\boldsymbol{\xi}}'_h \cdot \nabla_h^2 \boldsymbol{u}_h - \tilde{\zeta}\, w_{zz} - \tilde{\boldsymbol{\xi}}'_{hz} \cdot \nabla_h w, \tag{4.5}$$

which differs from (4.4) in the addition of the forcing terms including the vertical velocity $-\tilde{\zeta}\, w_{zz}$ and $-\tilde{\boldsymbol{\xi}}'_{hz} \cdot \nabla_h w$ (terms T_2 in (4.1)), that is, it includes all the terms

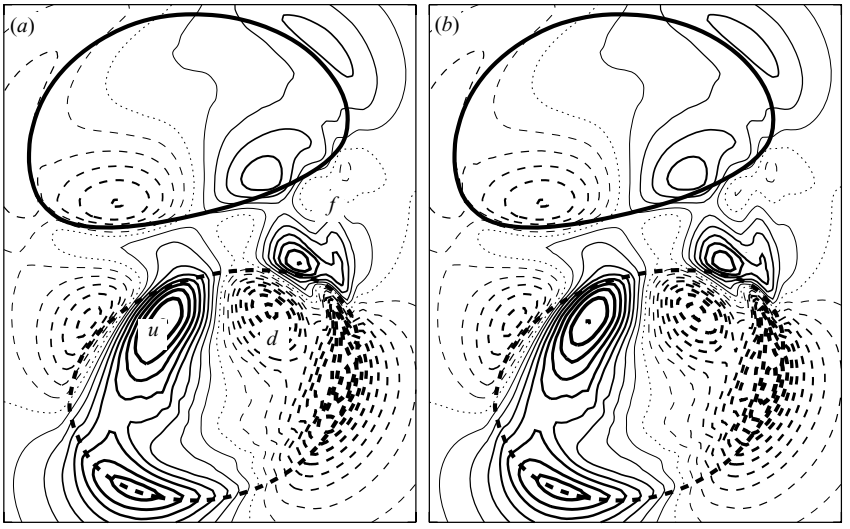

FIGURE 8. Horizontal distribution (C1) at $z \simeq -0.49$ ($i_Z = 59$) of (*a*) w^a ($w^a \in [-2.1, 1.8] \times 10^{-3}$); and (*b*) w^l ($w^l \in [-2.1, 1.8] \times 10^{-3}$). Contour interval $\delta w = 0.2 \times 10^{-3}$ and horizontal extent $(\delta x, \delta y) = (3.9, 4.9)c$, with the aspect ratio preserved. The labels *u* and *d* indicate the *w* extrema associated with the first wave of the frontal wave packet, while *f* indicates the larger wavenumber location of the frontal wave. The PV contours $\varpi = \pm 0.2$ are included for reference.

on the right-hand side of (4.1) except $c^2 \nabla_h \cdot (\mathscr{D}_z \nabla_h w)$ (term T_3) which is negligible. The solution w^v (figure 7*c*) reproduces well the QG extrema, and is therefore similar to w^q and w^{ql}. It displays two additional extrema, labelled *u* and *d*, which are due to the fact that the new terms in (4.5), $-\tilde{\zeta} w_{zz}$ and $-\tilde{\boldsymbol{\zeta}}'_{hz} \cdot \nabla_h w$, include now the total vertical velocity *w*, which in turn includes the *u* and *d* extrema. These terms are not responsible for the vertical velocity extrema *u* and *d* however since in w^v these extrema are clearly of smaller magnitude than those in the total *w* (figure 6*b*).

The next vertical velocity w^a (superscript *a* denotes advection) is a solution of the ω-equation including the same forcing terms as w^v plus the horizontal advection of $\tilde{\zeta}'_z$, that is, is solution of the almost complete steady ω-equation

$$\mathscr{L}^q\{w^a\} = 2\nabla_h \cdot \boldsymbol{Q}_h + \tilde{\boldsymbol{\zeta}}'_h \cdot \nabla_h^2 \boldsymbol{u}_h - \tilde{\zeta} w_{zz} - \tilde{\boldsymbol{\zeta}}'_{hz} \cdot \nabla_h w - \boldsymbol{u}_h \cdot \nabla_h \tilde{\zeta}'_z. \tag{4.6}$$

The field w^a (figure 8*a*) now reproduces both the QG extrema and the upwelling and downwelling regions on the anticyclone and dipole axis (labels *u* and *d*), as well as the frontal wave packet (label *f*). The vertical advection of $\tilde{\zeta}'_z$ and its local rate of change, terms $w\partial\tilde{\zeta}'_z/\partial z$ and $\partial\tilde{\zeta}'_z/\partial t$, respectively, in (4.1), have minor importance in the vertical motion of the upwelling and downwelling regions since the solution of (4.6) supplemented on the right-hand side by $-\partial\tilde{\zeta}'_z/\partial t - w\partial\tilde{\zeta}'_z/\partial z$ (field w^l in figure 8*b*) is very similar to w^a (figure 8*a*). The secondary importance of the local rate of change of $\tilde{\zeta}'_z$ is due to the smallness of the speed of displacement of the dipole ($O(U) \sim 0.1$) relative to the speed of the fluid particles ($O(u_h) \sim 1$). Therefore, the relevant quantity in the ω-equation associated with the vertical motion in the *u* and *d* regions is the material rate of change of $\tilde{\zeta}'_z$, and particularly, its horizontal advection. This is in contrast to the other *w* extrema ($Q\pm$ and $q\pm$) which have a QG origin. The material rate of change of $\tilde{\zeta}'_z$ is usually of secondary importance in balanced flows where there is a large cancellation between its horizontal advection and its local rate and

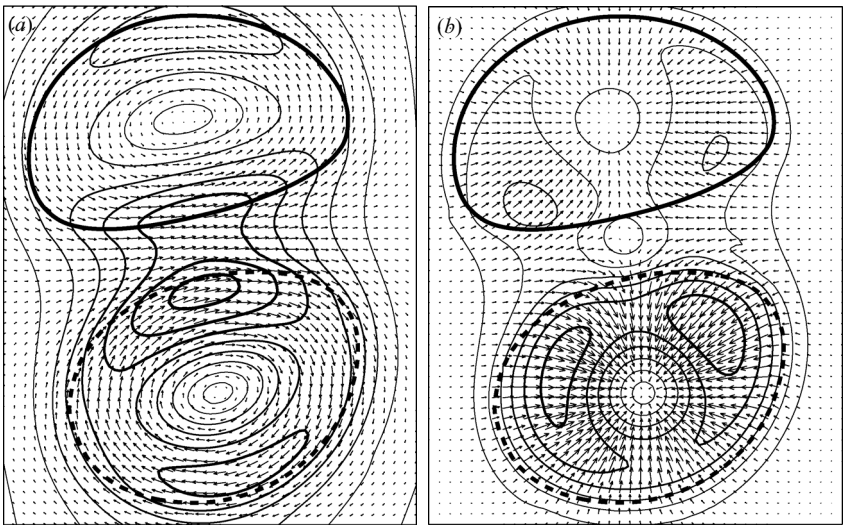

FIGURE 9. Horizontal distribution (C1) at $z=0$ ($i_Z=65$) of (a) $\boldsymbol{u}_h$ ($\max\{|\boldsymbol{u}_h|\}=2.1$, contour interval $\delta u_h=0.25$); (b) horizontal advective acceleration $\boldsymbol{u}_h\cdot\nabla_h\boldsymbol{u}_h$ ($\max\{|\boldsymbol{u}_h\cdot\nabla_h\boldsymbol{u}_h|\}=0.34$, contour interval $\delta=0.05$). Only every other vector is plotted.

change so that $\tilde{\zeta}_z'$ is approximately materially conserved (Viúdez & Dritschel 2003). This cancellation does not occur in the accelerating flow along the dipole axis.

5. The ageostrophic shear vorticity $\tilde{\zeta}_z'$

In the previous section we have seen the relevance of the material rate of change of $\tilde{\zeta}_z'$ in the generalized ω-equation and its relation with the vertical velocity. In this section we describe how the balanced flow in baroclinic dipoles is able to force large horizontal advection of $\tilde{\zeta}_z'$ in the dipole centre at shallow layers, and that the wave packet develops as a plane wave with variable wavenumber in the background flow at deeper layers.

5.1. *The ageostrophic shear vorticity in the dipole centre*

The rate of change of ageostrophic shear vorticity is related to the time interval a fluid particle takes to move along the dipole axis relative to the inertial period. Using (2.6a) we analyse $\tilde{\zeta}_z'$ from the behaviour of $\mathscr{A}_h=\boldsymbol{\omega}_h'$.

The magnitude of the horizontal velocity $u_h\equiv|\boldsymbol{u}_h|$ (figure 9a) has a maximum close to the dipole centre so that the fluid particles, inside and outside the PV vortices, accelerate before and decelerate after crossing the dipole centre. The horizontal advective acceleration is shown in figure 9(b). In C1 the larger accelerations occur inside the anticyclone. These maxima in the advective acceleration are due to both the normal centripetal acceleration κu_h^2, where $\kappa\equiv\boldsymbol{k}\cdot\nabla_h\times\boldsymbol{s}$ is the streamline curvature and $\boldsymbol{s}\equiv\boldsymbol{u}_h/u_h$ is the horizontal unit tangent vector, and the tangent advective acceleration $\frac{1}{2}\boldsymbol{s}\cdot\nabla_h u_h^2$.

Defining the horizontal normal vector $\boldsymbol{n}\equiv\boldsymbol{k}\times\boldsymbol{s}$, and neglecting the local acceleration and vertical advection, the rotation of the ageostrophic velocity $\boldsymbol{u}_h'\equiv\boldsymbol{u}_h-\boldsymbol{u}_h^g$ is

$$f\boldsymbol{k}\times\boldsymbol{u}_h'\cong-\boldsymbol{u}_h\cdot\nabla_h\boldsymbol{u}_h=-\frac{1}{2}\frac{\delta u_h^2}{\delta s}\boldsymbol{s}-\kappa u_h^2\boldsymbol{n},\tag{5.1}$$

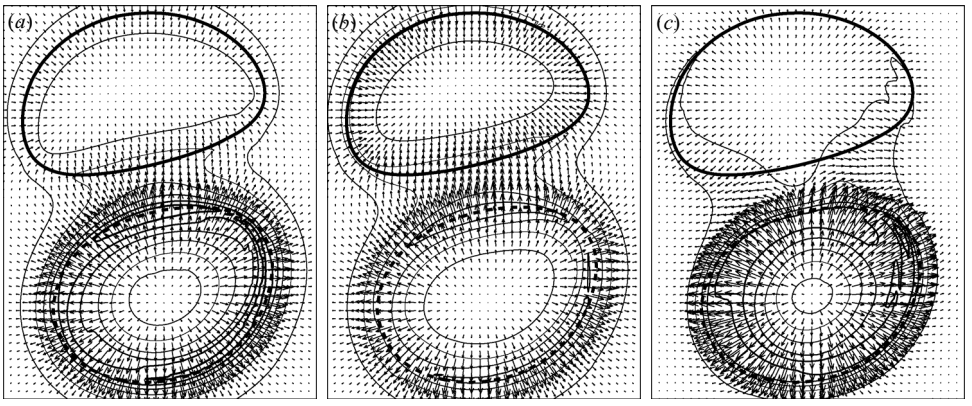

FIGURE 10. Horizontal distribution (C1) at $z \simeq -0.49$ ($i_Z = 59$) of (*a*) $\tilde{\boldsymbol{\omega}}_h$ ($\max\{|\tilde{\boldsymbol{\omega}}_h|\} = 3.4$, $\delta = 0.5$), (*b*) $\tilde{\boldsymbol{\omega}}_h^g = c^2 \nabla_h \mathscr{D}$ ($\max\{|\tilde{\boldsymbol{\omega}}_h^g|\} = 2.5$, $\delta = 0.5$), and (*c*) $\mathscr{A}_h = \tilde{\boldsymbol{\omega}}_h'$ ($\max\{|\mathscr{A}_h|\} = 1.3$, $\delta = 0.2$). Only every other vector is plotted.

where $\delta/\delta s \equiv \boldsymbol{s} \cdot \nabla_h$ is the directional derivative along $\boldsymbol{s}$. The normal component of (5.1) is the centripetal acceleration

$$f\boldsymbol{n} \cdot (\boldsymbol{k} \times \boldsymbol{u}_h') = f\boldsymbol{s} \cdot \boldsymbol{u}_h' = fu_s' = f(u_h - u_s^g) \cong -\kappa u_h^2, \tag{5.2}$$

where $u_s^g \equiv \boldsymbol{s} \cdot \boldsymbol{u}_h^g$ is the alongstream component of $\boldsymbol{u}_h^g$. The quantity $|\kappa| u_h^2$ is the *centripetal acceleration* magnitude. Thus, in the vortices away from the dipole axis, the flow is *supergeostrophic* ($u_s' > 0$) in the anticyclone ($\kappa < 0$), but *subgeostrophic* ($u_s' < 0$) in the cyclone ($\kappa > 0$).

The tangent component of (5.1) is

$$f\boldsymbol{s} \cdot (\boldsymbol{k} \times \boldsymbol{u}_h') = -f\boldsymbol{n} \cdot \boldsymbol{u}_h' = -fu_n' = fu_n^g \cong -\tfrac{1}{2} \frac{\delta u_h^2}{\delta s}, \tag{5.3}$$

where $u_n^g \equiv \boldsymbol{n} \cdot \boldsymbol{u}_h^g$ is the cross-stream component of $\boldsymbol{u}_h^g$. The quantity $\frac{1}{2}|\delta u_h^2/\delta s|$ is the *speed acceleration* magnitude. Thus, along the dipole axis where $\kappa \cong 0$, in the flow $u_n' = -u_n^g > 0$ in the rear region where $\delta u_h^2/\delta s > 0$, but $u_n' = -u_n^g < 0$ in the frontal region where $\delta u_h^2/\delta s < 0$.

As a consequence, the rotated ageostrophic velocity

$$\boldsymbol{k} \times \boldsymbol{u}_h' = \boldsymbol{k} \times (u_s'\boldsymbol{s} + u_n'\boldsymbol{n}) = -u_n'\boldsymbol{s} + u_s'\boldsymbol{n},$$

points out from the vortex cores in the vortical region away from the dipole axis, where the curvature acceleration dominates over the speed acceleration (thus $|u_s'| > |u_n'|$). However, $\boldsymbol{k} \times \boldsymbol{u}_h'$ is counter flow at the entrance, and along flow at the dipole exit, on the along-dipole line where the speed acceleration dominates over the curvature acceleration (thus $|u_n'| > |u_s'|$).

The above results concerning $\boldsymbol{k} \times \boldsymbol{u}_h$, $\boldsymbol{k} \times \boldsymbol{u}_h^g$, and $\boldsymbol{k} \times \boldsymbol{u}_h'$ apply also to $\tilde{\boldsymbol{\omega}}_h$, $\tilde{\boldsymbol{\omega}}_h^g$, and $\tilde{\boldsymbol{\omega}}_h'$, respectively (figure 10). This is so because, neglecting the vertical velocity contribution, it follows that $\tilde{\boldsymbol{\omega}}_h \simeq \boldsymbol{k} \times \tilde{\boldsymbol{u}}_{hz}$, where $\tilde{\boldsymbol{u}}_{hz} \equiv \partial \tilde{\boldsymbol{u}}_h / \partial z$. The vertical shear $\boldsymbol{u}_{hz} = u_{hz}\boldsymbol{s} + u_h \Theta_Z \boldsymbol{n}$, where $\Theta_Z \equiv \boldsymbol{n} \cdot \partial \boldsymbol{s}/\partial z$ is the *backing* or horizontal rotation of $\boldsymbol{u}_h$ along the vertical $\boldsymbol{k}$-line. In mesoscale oceanic flows, where isopycnals are approximately tangent to the flow, the backing term $u_h \Theta_Z$ is usually smaller than the shear speed $u_{hz} \equiv \partial u_h / \partial z$, so that $\boldsymbol{u}_{hz}$ points mainly in the same direction as $\boldsymbol{u}_h$ (the horizontal velocity increases with z in the lower half of the vortex, $z < 0$). Therefore $\tilde{\boldsymbol{\omega}}_h'$ is in the same direction as $\boldsymbol{k} \times \boldsymbol{u}_h'$. In C2 these distributions

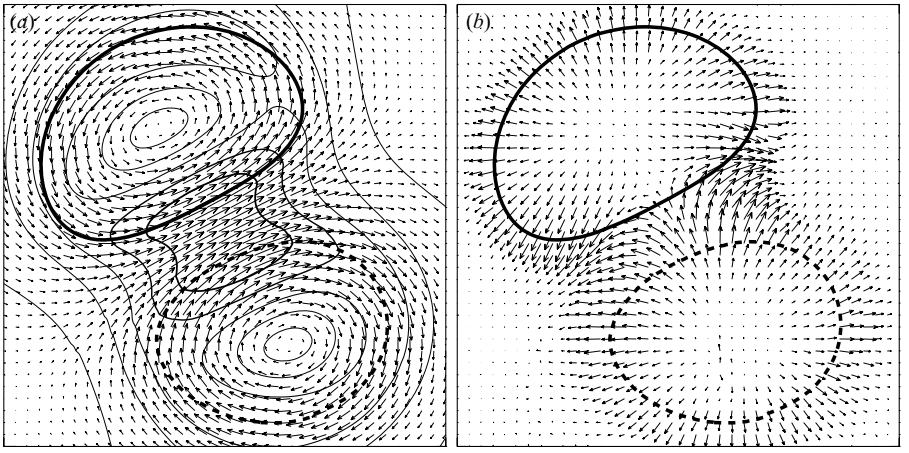

FIGURE 11. Horizontal distribution (C2) at $z=-0.21$ ($i_Z=240$) of (*a*) $\boldsymbol{u}_h$ ($\max\{|\boldsymbol{u}_h|\}=3.0$, $\delta u_h=0.5$); and (*b*) $\mathscr{A}_h=\tilde{\boldsymbol{\omega}}'_h$ ($\max\{|\mathscr{A}_h|\}=0.98$). Only every 10 vectors is plotted.

(figure 11) have qualitatively a similar behaviour, though in this case the horizontal speed (figure 11*a*) has a greater axial symmetry than in C1 (figure 9*a*).

The crucial point relative to the frontal wave generation, and to the upwelling and downwelling areas *u* and *d*, is the pattern of $\mathscr{A}_h=\boldsymbol{\omega}'_h$ along the dipole axis. Owing to the ageostrophic motion explained above, the vector $\mathscr{A}_h$ rotates anticyclonically as the fluid particle moves along the dipole axis. This is clearly visible in C2 (figure 11*b*), and more noticeable on the anticyclonic side of the dipole axis in C1 (figure 10*c*). When this rotation is performed in a time period close to the inertial period (or Rossby number $|\mathscr{R}|$ approaching 1), this ageostrophic motion can be the 'first push' triggering the IGWs. The scaling of the frontal wave amplitude with the Rossby number is an open question however. Thus, IGW generation is favoured on the anticyclonic side of the along-dipole line, where the anticyclonic rotation of $\mathscr{A}_h$ is increased in the dipole core thanks to the additional contribution from the negative curvature acceleration. We note that, like the horizontal velocity $\boldsymbol{u}_h$ (A 4*a*), the rate of change of $\mathscr{A}_h$ (2.3) displays an anticyclonic inertial mode when *w* and the nonlinear terms on the right-hand side of (2.3) are small.

The above ageostrophic patterns imply that $\mathscr{A}_h$ is divergent ($\nabla_h\cdot\mathscr{A}_h>0$) at the dipole centre and, from (2.6*a*), that ζ'_z has a relative minimum (black symbol in figure 12*a*). This implies that a fluid particle moving along the dipole axis experiences a decrease of ζ'_z ($\mathrm{d}\zeta'_z/\mathrm{d}t<0$) as it approaches the dipole centre, and an increase of ζ'_z ($\mathrm{d}\zeta'_z/\mathrm{d}t>0$) as it leaves the dipole centre. By virtue of (4.1) this implies a contribution of $\mathscr{L}^q\{w\}\equiv c^2\nabla_h^2 w+w_{zz}<0$ immediately before, and $\mathscr{L}\{w\}^q>0$ immediately after, respectively, the dipole centre. This in turn implies, since $w=0$ at $z=0$, that $w>0$ and $w<0$, respectively, in these areas, which correspond to the upwelling and downwelling regions labelled *u* and *d*. We note that, owing to the presence of the short-scale waves in the distribution of ζ'_z (figure 12*a*), the large-scale contribution of the advection of ζ'_z would be largely hidden in a figure displaying the distribution of $\mathrm{d}\zeta'_z/\mathrm{d}t$ or $\boldsymbol{u}_h\cdot\nabla_h\zeta'_z$, unless a spatial average filter is applied to smooth the short scales. For this reason it is preferable to analyse the importance of this term in *w* by solving the ω-equation (4.1) which, implying a second order spatial integration, acts as a filter of the short-scales.

An alternative way of inferring the *w* pattern from the distribution of $\mathscr{A}_h$ is from (2.6*b*) taking into account that $\nabla^2 w\simeq\partial^2 w/\partial z^2$. The horizontal vector field $\mathscr{A}_h$ (figure 11*b*) has a curl with vertical component positive at the rear side, and negative

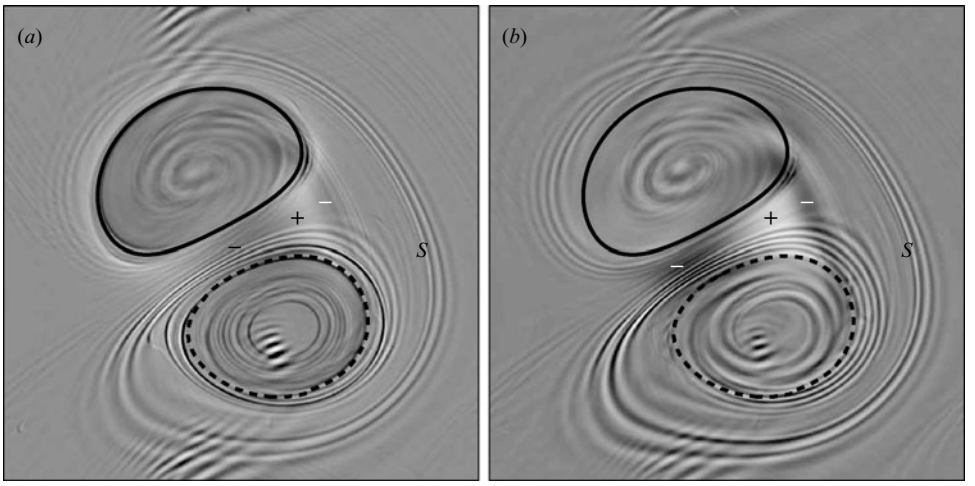

FIGURE 12. Horizontal distribution (C2) at $z=-0.21$ ($i_Z=240$) of (a) $\tilde{\zeta}'_z=-\nabla_h\cdot\mathscr{A}_h$ ($\tilde{\zeta}'_z\in[-2.0, 1.9]$); and ($b$) $\nabla^2\tilde{w}=-\boldsymbol{k}\cdot\nabla_h\times\mathscr{A}_h$ ($\nabla^2\tilde{w}\in[-0.74, 0.60]$).

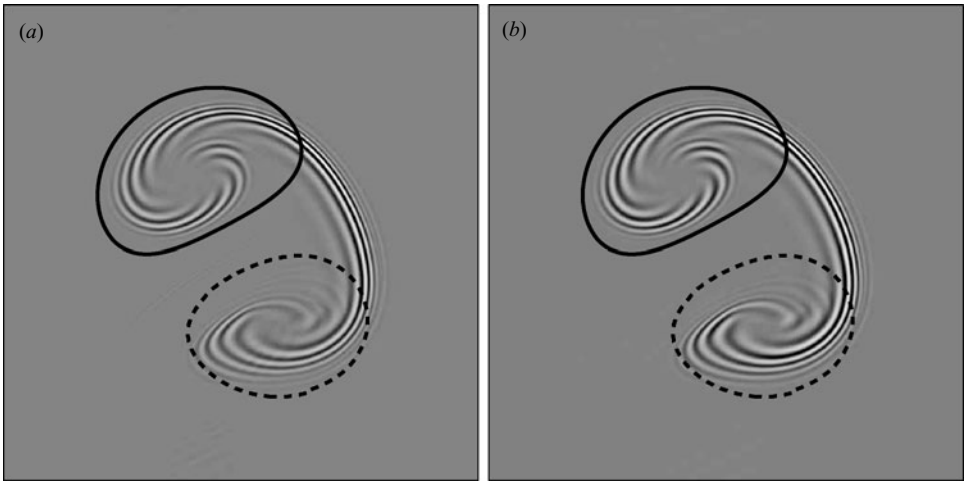

FIGURE 13. Horizontal distribution (C2) at $z\simeq-1.2$ ($i_Z=160$) of (a) $\tilde{\zeta}'_z=-\nabla_h\cdot\mathscr{A}_h$ ($\tilde{\zeta}'_z\in[-37, 39]$); and ($b$) $\nabla^2\tilde{w}=-\boldsymbol{k}\cdot\nabla_h\times\mathscr{A}_h$ ($\nabla^2\tilde{w}\in[-23, 24]$).

at the frontal side, of the dipole axis. This implies $\nabla^2 w<0$ (black 'minus' symbol in figure 12b) and therefore $w>0$ at the rear side (upwelling region u), with the opposite sign (black symbol + in figure 12b) at the frontal side (downwelling region d).

A second minimum in $\tilde{\zeta}'_z$, of smaller length scale, occurs in shallow layers at the frontal side of the dipole axis (white 'minus' symbol in figure 12a), but the wave front is not further amplified at this depth. Instead, the wave perturbation is transmitted to the deep layers and amplifies at the frontal side of the dipole, where stationary – relative to the moving dipole – plane wave solutions with variable wavenumber in the background flow are possible. These solutions require that the vertical shear of the along-dipole component of the horizontal velocity, $\partial u/\partial z$ (aligning the x-axis along the dipole axis) be similar to $-N/f$ times its along-dipole derivative, $\partial u/\partial x$ (Viúdez

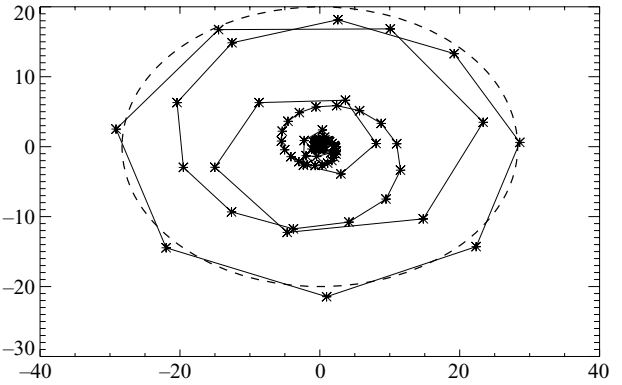

FIGURE 14. Scatterplot of $\nabla^2\tilde{w}$ (y-axis) versus $\tilde{\zeta}_z'$ (x-axis) along the line $(y, z) = (0, -0.2)$ in C2. The large values correspond to the points on the horizontal line intersecting the frontal wave packet. The axes aspect ratio is preserved. The dashed closed curve is an ellipse with semi-axes $(a_X, a_Y) = 20(\sqrt{2}, 1)$.

2007). In deeper layers the frontal wave packet therefore appears neatly at the front of the dipole in both $\tilde{\zeta}_z'$ and $\nabla^2 w$ distributions (figure 13).

5.2. *Phase relations between $\tilde{\zeta}_z'$ and $\nabla^2 w$ in the frontal wave packet*

In mid-layers the frontal wave packet approximately satisfies plane wave solutions with variable wavenumber in the background flow, as is deduced from the phase relations between $\tilde{\zeta}_z'$ and $\nabla^2 w$ described next. These phase relations can be obtained from the complex plane wave solutions $\hat{\chi}(\boldsymbol{x}, t) \equiv \hat{\chi}_0 \exp(\mathrm{i}\theta(\boldsymbol{x}, t))$, where the phase $\theta(\boldsymbol{x}, t) \equiv \boldsymbol{k} \cdot \boldsymbol{x} - \omega_l t$, the wavenumber $\boldsymbol{k} = (k, l, m) \equiv \nabla\theta$, and the local (or absolute) frequency $\omega_l \equiv -\partial\theta/\partial t$. As a function of $\hat{\mathscr{D}}$ the plane waves imply

$$\hat{\boldsymbol{u}}_h = (\hat{u}, \hat{v}) = f\frac{m}{k_h^2}\left(-l + \mathrm{i}k\,\frac{\omega_p}{f}, k + \mathrm{i}l\,\frac{\omega_p}{f}\right)\hat{\mathscr{D}}, \quad \hat{w} = -\mathrm{i}\,\omega_p\,\hat{\mathscr{D}}, \tag{5.4a, b}$$

$$\nabla^2\hat{w} = \mathrm{i}K^2\,\omega_p\,\hat{\mathscr{D}} \quad \frac{\hat{\zeta}}{f} = \mathrm{i}m\,\hat{\mathscr{D}}, \tag{5.4c, d}$$

$$\frac{\hat{\zeta}_z^g}{f} = c^2 k_h^2\,\hat{\mathscr{D}}, \quad \frac{\hat{\zeta}_z'}{f} = -K^2\left(\frac{\omega_p}{f}\right)^2\hat{\mathscr{D}}, \tag{5.4e, f}$$

$$\hat{\boldsymbol{\mathscr{A}}}_h = (\hat{\mathscr{A}}, \hat{\mathscr{B}}) = \frac{K^2}{k_h^2}\frac{\omega_p}{f}\left(l - \mathrm{i}k\,\frac{\omega_p}{f}, -k - \mathrm{i}l\,\frac{\omega_p}{f}\right)\hat{\mathscr{D}} = -\frac{K^2}{m}\frac{\omega_p}{f^2}\,\hat{\boldsymbol{u}}_h \tag{5.4g}$$

where the squared horizontal wavenumber $k_h^2 \equiv k^2 + l^2$, squared total wavenumber $K^2 \equiv k_h^2 + m^2$, and the frequency relative to the fluid particle $\omega_p \equiv -\mathrm{d}\theta/\mathrm{d}t$ (or intrinsic) satisfies the dispersion relation

$$\omega_p^2 = \frac{k_h^2 N^2 + m^2 f^2}{K^2}.$$

Relations (5.4) correspond to the usual plane wave solutions except that the frequency relative to the fluid particle ω_p is used instead of the local frequency ω_l. Aligning the x-axis along the dipole axis ($l = 0$) these relations are approximate solutions with horizontal and vertical wavenumbers k and m that depend on the

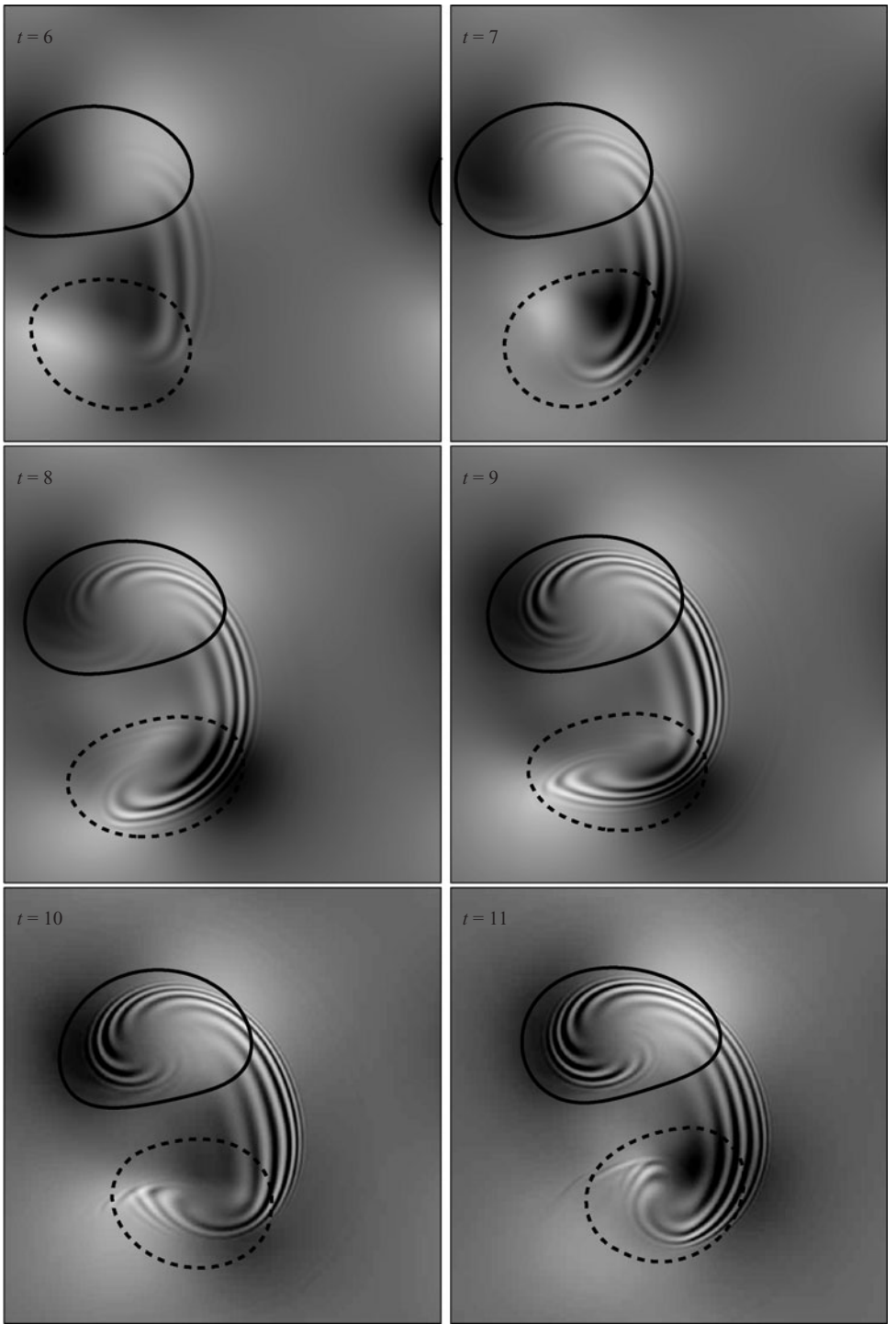

FIGURE 15. For caption see facing page.

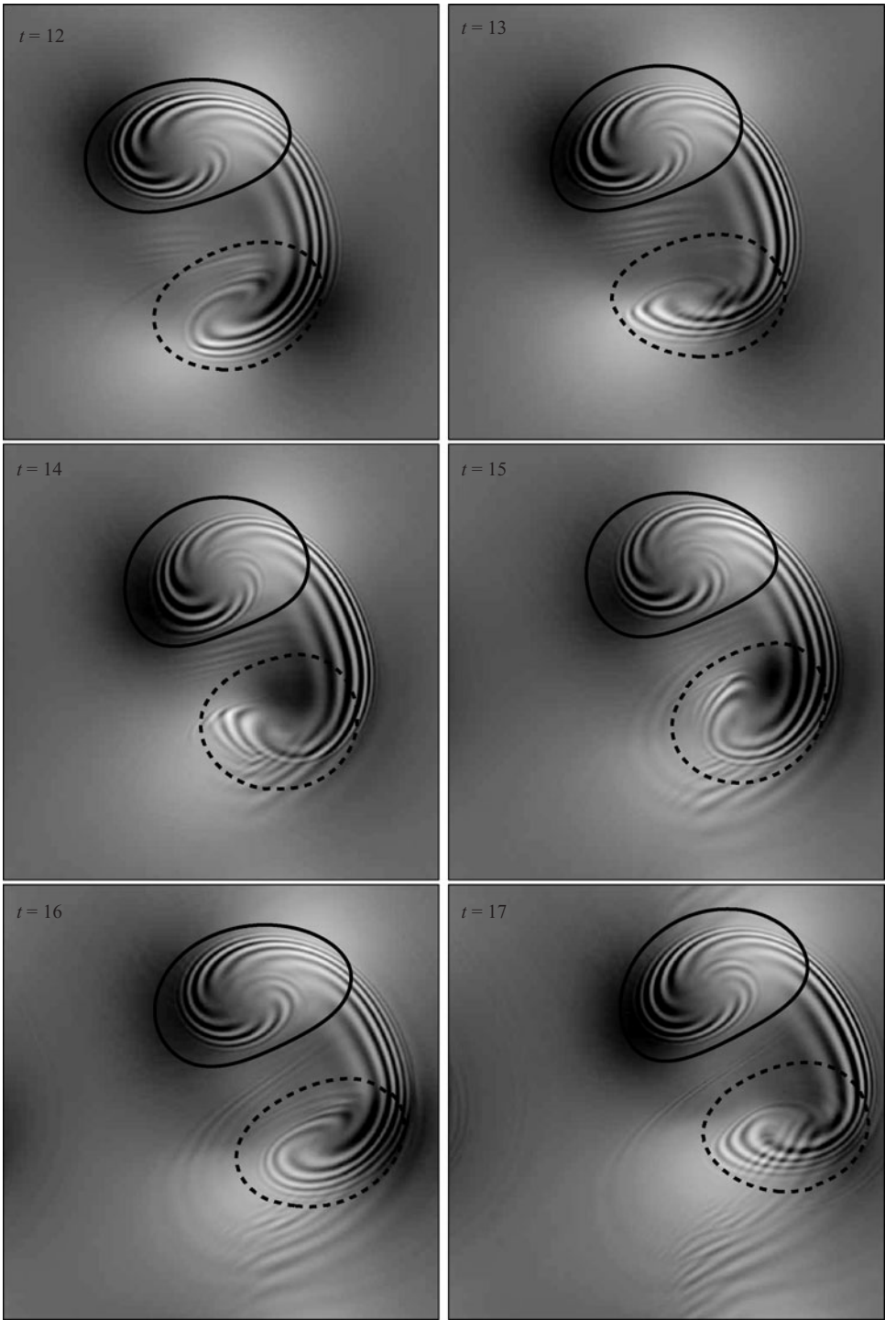

FIGURE 15. Time evolution of $w(x, y)$ at $z = -1.18$ ($i_Z = 161$) for C2. Time in T_{ip}, $w \in [-5.4, 7.5] \times 10^{-3}$.

background horizontal flow,

$$k(x,z) = -\frac{\omega_p}{u(x,z) - U}, \quad \frac{m(x,z)}{-k(x,z)} = c \quad \Rightarrow \omega_p^2 = \frac{2f^2}{1+c^{-2}} \cong 2f^2, \tag{5.5}$$

where U is the speed of displacement of the dipole. The above relations assume that the wave frequency relative to the dipole reference frame is zero (that is, that the frontal wave packet remains stationary in this frame), so that the advection of the wave phase by the background flow relative to the dipole reference frame $(u-U)k = (u-U)\,\partial\theta/\partial x$ equals $-\omega_p$. Since ω_p is constant, if u decreases along the dipole axis then k has to increase. This kinematic effect is similar to that of a pendulum oscillating with constant frequency along the y-axis and simultaneously moving with velocity u along the x-axis. Kinematically, as u slowly decreases, the wavenumber in the x-direction (k) must increase since the x-distance per unit time (proportional to the oscillating period) decreases.

Relations (5.5) imply the ratio

$$\frac{\hat{\tilde{\zeta}}_z'}{\nabla^2\hat{\tilde{w}}} = \frac{\nabla_h \cdot \hat{\mathscr{A}}_h}{\boldsymbol{k} \cdot \nabla_h \times \hat{\mathscr{A}}_h} = \mathrm{i}\frac{\omega_p}{f} \cong \mathrm{i}\sqrt{2}. \tag{5.6}$$

There is therefore a phase difference of $\pi/2$ between the wave distributions of $\tilde{\zeta}_z'$ and $\nabla^2\tilde{w}$, with the amplitude of $\tilde{\zeta}_z'$ approximately $\sqrt{2}$ times larger than the amplitude of $\nabla^2\tilde{w}$, as can be inferred from a scatterplot of the values of $\nabla^2\tilde{w}$ versus $\tilde{\zeta}_z'$ along the dipole axis at mid depth (figure 14). Note that the ratio $\sqrt{2}$ is preserved as the wavenumber k changes.

6. Time evolution of the frontal wave packet

The unsteady generation of the frontal wave packet at mid depth can be followed from the time series of w during 12 inertial periods (figure 15) and interpreted in a way consistent with the hypothesis that the wave originates in the shallow layers. From $t = 6\,T_{ip}$ to $t = 7\,T_{ip}$ the wave packet develops at mid depth with amplitude growing first in the frontal part of the dipole, as the wave is carried downwards by pressure perturbations, and horizontally forward in an advective way by the fast particles moving along the dipole axis. Simultaneously with the wave motion, the fluid particles also experience the balanced vertical velocity of the mesoscale background dipolar flow, namely the quadrupolar pattern seen in these images as four large-scale light and dark areas at the apices of the vortices.

As the amplitude of the frontal wave packet continues increasing (from $t = 8\,T_{ip}$ to $9\,T_{ip}$) the wave is introduced into the vortices by the rotating, slower moving fluid particles which acquired the wave perturbation when they were located close to the dipole axis. The wave amplitude develops in the vortices both tangentially, that is circularly as the wave is carried in an advective way by the oscillating fluid particles, as well as normally, that is towards the vortex centres by pressure perturbations. Therefore the wave spiralling inside the vortices develops over a time interval longer than the time the frontal wave takes to develop ahead of the dipole. The spiral wave takes at least $8\,T_{ip}$ (from $t = 5\,T_{ip}$ to $t = 13\,T_{ip}$) to completely develop.

The development of the spiralling of the frontal wave packet inside the vortices occurs more smoothly in the cyclone than in the anticyclone. This is because, in this case, the anticyclone experiences, more violently than the cyclone, the phase

oscillations appropriate to the dipole heading, which involves changes in the geometry of the vortices. The dipole heading has a period of approximately $4\,T_{ip}$. Every heading period the cyclone emits spontaneously two bursts of small-amplitude IGWs that propagate away from the vortical flow as wave packets. A first burst is emitted northward towards the dipole axis at $t = 10$–$11\,T_{ip}$ and, $4\,T_{ip}$ later, at $t = 14$–$15\,T_{ip}$. The second wave packet is radiated southward off the dipole at $t = 13\,T_{ip}$ and, $4\,T_{ip}$ later, at $t = 17\,T_{ip}$.

7. Concluding remarks

In rotating stably stratified flows the baroclinic dipole is a paradigmatic case of a coherent vortex structure where the largely ageostrophic, but otherwise balanced, flow spontaneously generates a stationary, relative to the dipole frame of reference, packet of inertia–gravity waves. It is suggested here that the short-scale frontal wave packet, clearly identified from the background flow at mid-depths, is originated by the large-scale balanced flow in the shallow layers, owing to the sudden acceleration and deceleration experienced by the fluid particles as they move along, or close to, the dipole axis. The IGW generation is favoured on the anticyclonic side of the dipole axis thanks to the combined effect of the speed and centripetal accelerations which causes an anticyclonic rotation of the horizontal ageostrophic vorticity vector in a time scale of about one inertial period. It is therefore inferred that the frontal wave packet first originates when the horizontal advective acceleration becomes large enough to become comparable with, though still smaller than, the Coriolis acceleration. When this happens the velocity time scale, relative to the fluid particle, is close to the inertial period, so that inertia–gravity waves with frequency close to the inertial frequency are amplified in the frontal part of the dipole and inside the vortices wherever these are dynamically allowed by the background vortical flow.

Since the initial wave excitation only contributes to the total density and three-dimensional velocity fields as a small perturbation, the origin and development of the frontal wave packet is better observed in ageostrophic variables of smaller magnitude, like the differential ageostrophic component of the vertical vorticity or the Laplacian of the vertical velocity. An analysis of the rate of change of the differential ageostrophic vorticity of the fluid particle (the ω-equation) shows that this material rate of change is as large, in some places, as the larger QG terms in the ω-equation. In balanced dynamics the material rate of change of ageostrophic vorticity is of second order in the ω-equation however. The large amplitudes of this rate of change at the dipole axis suggest that they are in fact the initial stages of the frontal wave packet, with the only difference that their spatial scales are larger than the short-scale wavelengths of the fully developed frontal wave packet ahead of the dipole at mid-depths.

The amplitude of the wave packet is effectively enhanced when the ratio between the relative acceleration and the Coriolis acceleration becomes close to unity, or Rossby number approaching 1, though the development of a weaker frontal wave packet does not require the flow to become inertially unstable. Thus, the frontal wave packet, having a wave momentum opposite to the dipole's, effectively reduces the speed of displacement of the dipole even before the limit of inertial instability is reached.

Computer resources and technical assistance provided by the Barcelona Supercomputing Center-*Centro Nacional de Supercomputación*, and comments from three anonymous reviewers are gratefully acknowledged.

Appendix. Theoretical basis of the numerical model

A.1. *Basic equations*

We consider the isochoric (volume-preserving) motion of a stable stratified fluid in a reference frame rotating with constant angular velocity $f/2$ around the vertical z-axis with respect to an inertial frame. The density anomaly ρ' is defined as

$$\rho'(\boldsymbol{x},t) \equiv \rho(\boldsymbol{x},t) - \varrho_Z\, z - \rho_0, \tag{A 1}$$

where ρ is the mass density, and $\rho_0 > 0$ and $\varrho_Z < 0$ are given constants. We introduce the pressure anomaly p' as the pressure p (including the centripetal potential) minus the hydrostatic pressure due to a constant vertical density stratification

$$p'(\boldsymbol{x},t) \equiv p(\boldsymbol{x},t) + g\left(\rho_0 + \tfrac{1}{2}\varrho_Z z\right) z, \tag{A 2}$$

where g is the acceleration due to gravity. The Boussinesq approximation in the vertical component of the momentum equation is

$$-\frac{1}{\rho}\left(\frac{\partial p}{\partial z} - g\rho\right) \cong -\alpha_0\left(\frac{\partial p}{\partial z} - g\rho\right) = -\alpha_0\frac{\partial p'}{\partial z} - \alpha_0 g\rho', \tag{A 3}$$

where $\alpha_0 \equiv \rho_0^{-1}$ is a constant specific volume. Vector components here always refer to Cartesian components. The basic equations are the non-hydrostatic balance of linear momentum in a rotating frame under the f-plane and Boussinesq approximations, the mass conservation equation, and the isochoric condition:

$$\frac{\mathrm{d}\boldsymbol{u}_h}{\mathrm{d}t} + f\boldsymbol{k}\times\boldsymbol{u}_h = -\alpha_0\nabla_h p', \tag{A 4a}$$

$$\frac{\mathrm{d}w}{\mathrm{d}t} = -\alpha_0\frac{\partial p'}{\partial z} - \alpha_0 g\rho', \tag{A 4b}$$

$$\frac{\mathrm{d}\rho}{\mathrm{d}t} + \rho\,\nabla\cdot\boldsymbol{u} = 0, \tag{A 4c}$$

$$\nabla\cdot\boldsymbol{u} = 0. \tag{A 4d}$$

The initial unknowns are the three-dimensional velocity field (u, v, w), the pressure anomaly p', and the density anomaly ρ'. Symbol $\mathrm{d}(\,)/\mathrm{d}t \equiv \partial(\,)/\partial t + \boldsymbol{u}\cdot\nabla(\,)$ denotes the material time derivative (in the rotating frame).

A.2. *Mass conservation*

It is convenient to express ρ in terms of the field d defined by

$$d \equiv (\rho - \rho_0)/\varrho_Z; \tag{A 5}$$

$d(\boldsymbol{x},t)$ represents the depth, or vertical location, that an isopycnal located at $\boldsymbol{x}$ at time t has in the reference density configuration defined by $\rho_0 + \varrho_Z z$. Thus, the density field is expressed in terms of distances. The displacement $\mathscr{D}$ of isopycnals with respect to the reference density configuration is defined as

$$\mathscr{D}(\boldsymbol{x},t) \equiv z - d(\boldsymbol{x},t). \tag{A 6}$$

$\mathscr{D}(\boldsymbol{x},t)$ is the vertical displacement of the isopycnal currently located at $(\boldsymbol{x},t)$ with respect to its reference position. The incompressibility condition $\mathrm{d}\rho/\mathrm{d}t = \mathrm{d}(d)/\mathrm{d}t = 0$

is expressed in terms of $\mathscr{D}$ as

$$\frac{\mathrm{d}\mathscr{D}}{\mathrm{d}t} = w. \tag{A 7}$$

The vertical displacement of isopycnals $\mathscr{D}$ is related to ρ by

$$N^2(\mathscr{D}(\boldsymbol{x}, t) - z) = g\left(\frac{\rho(\boldsymbol{x}, t)}{\rho_0} - 1\right), \tag{A 8}$$

where $N^2 \equiv -\alpha_0 g \varrho_Z$ is the square of the constant background Brunt–Väisälä frequency.

A.3. *Geostrophic quantities*

For any quantity χ let $\tilde{\chi} \equiv \chi/f$. The geostrophic velocity shear is defined through the thermal wind expression

$$\frac{\partial \tilde{\boldsymbol{u}}^g}{\partial z} \equiv -c^2 \boldsymbol{k} \times \nabla_h \mathscr{D} = c^2 \left(\frac{\partial \mathscr{D}}{\partial y}, -\frac{\partial \mathscr{D}}{\partial x}\right), \tag{A 9}$$

where $c = \epsilon^{-1} \equiv N/f$. The relative pseudovorticity is the vorticity of the horizontal velocity, defined in Cartesian components as

$$\boldsymbol{\zeta} \equiv \nabla \times \boldsymbol{u}_h = \left(-\frac{\partial v}{\partial z}, \frac{\partial u}{\partial z}, \frac{\partial v}{\partial x} - \frac{\partial u}{\partial y}\right). \tag{A 10}$$

The horizontal gradient of $\mathscr{D}$ (times c^2) may be interpreted as the dimensionless horizontal geostrophic pseudovorticity

$$\tilde{\boldsymbol{\xi}}_h^g = \left(-\frac{\partial \tilde{v}^g}{\partial z}, \frac{\partial \tilde{u}^g}{\partial z}\right) = \tilde{\boldsymbol{\omega}}_h^g = c^2 \nabla_h \mathscr{D}. \tag{A 11}$$

Since $\boldsymbol{\zeta}$ is solenoidal ($\nabla \cdot \boldsymbol{\zeta} = 0$) the horizontal divergence of $\tilde{\boldsymbol{\xi}}_h^g$ is equal to (minus) the differential geostrophic vertical vorticity,

$$-\nabla_h \cdot \tilde{\boldsymbol{\xi}}_h^g = \frac{\partial}{\partial z}\left(\frac{\partial \tilde{v}^g}{\partial x} - \frac{\partial \tilde{u}^g}{\partial y}\right) = \frac{\partial \tilde{\zeta}^g}{\partial z} = \tilde{\zeta}_z^g = -c^2 \nabla_h^2 \mathscr{D}. \tag{A 12}$$

Using (A 7) it follows that the rate of change of $\nabla \mathscr{D}$ is

$$\frac{\mathrm{d}}{\mathrm{d}t} \nabla \mathscr{D} = \nabla w - \nabla \boldsymbol{u} \cdot \nabla \mathscr{D}. \tag{A 13}$$

The horizontal component of the above equation expresses the rate of change of $\tilde{\boldsymbol{\xi}}_h^g$. It is used below to obtain the rate of change of the dimensionless horizontal ageostrophic vorticity $\tilde{\boldsymbol{\omega}}_h' \equiv \tilde{\boldsymbol{\omega}}_h - \tilde{\boldsymbol{\omega}}_h^g = \tilde{\boldsymbol{\omega}}_h - c^2 \nabla_h \mathscr{D}$, where the relative vorticity $\boldsymbol{\omega} \equiv \nabla \times \boldsymbol{u}$.

A.4. *The vorticity equation*

The vorticity equation consistent with (A 4) is

$$\frac{\mathrm{d}\tilde{\boldsymbol{\omega}}}{\mathrm{d}t} = \tilde{\boldsymbol{\omega}} \cdot \nabla \boldsymbol{u} + \frac{\partial \boldsymbol{u}}{\partial z} + f c^2 \boldsymbol{k} \times \nabla_h \mathscr{D}, \tag{A 14}$$

and is used next to express the material rate of change of $\tilde{\boldsymbol{\omega}}_h'$.

A.5. *The horizontal ageostrophic vorticity potentials*

The three-dimensional vector potential $\boldsymbol{\varphi} = (\varphi, \psi, \phi)$ and its Laplacian $\mathscr{A}$ are introduced by the definitions

$$\mathscr{A} = (\mathscr{A}, \mathscr{B}, \mathscr{C}) \equiv \nabla^2 \boldsymbol{\varphi} = (\nabla^2 \varphi, \nabla^2 \psi, \nabla^2 \phi) \equiv \tilde{\boldsymbol{\omega}} - c^2 \nabla \mathscr{D}. \tag{A 15}$$

From the divergence of (A 15), and using the vector identity

$$\nabla^2\boldsymbol{\varphi} = \nabla(\nabla\cdot\boldsymbol{\varphi}) - \nabla\times\nabla\times\boldsymbol{\varphi}, \tag{A 16}$$

we obtain

$$c^2\mathscr{D} = -\nabla\cdot\boldsymbol{\varphi}, \quad \tilde{\boldsymbol{u}} = -\nabla\times\boldsymbol{\varphi}. \tag{A 17a, b}$$

Thus, $c^2\mathscr{D}$ is the source of $-\boldsymbol{\varphi}$, and $-\boldsymbol{\varphi}$ is the velocity potential of $\tilde{\boldsymbol{u}}$. Consequently, $c^2\mathscr{D}$ may be interpreted as the source of the velocity potential of $\tilde{\boldsymbol{u}}$. Because of (A 11), the horizontal vector $\mathscr{A}_h = (\mathscr{A}, \mathscr{B})$ is the dimensionless horizontal ageostrophic vorticity

$$\mathscr{A}_h = \nabla^2\boldsymbol{\varphi}_h = \tilde{\boldsymbol{\omega}}_h - \tilde{\boldsymbol{\omega}}_h^g = \tilde{\boldsymbol{\omega}}_h'. \tag{A 18}$$

Combining (A 13) with (A 14), the rate of change of $\mathscr{A}$ is

$$\frac{\mathrm{d}\mathscr{A}}{\mathrm{d}t} = -f\boldsymbol{k}\times\mathscr{A}_h + (1-c^2)\nabla w + \tilde{\boldsymbol{\omega}}\cdot\nabla\boldsymbol{u} + c^2\nabla\boldsymbol{u}\cdot\nabla\mathscr{D}. \tag{A 19}$$

The horizontal component of (A 19) is (2.3). The main advantages of these prognostic equations is that they allow us to use the potential vector $\boldsymbol{\varphi}$ so that volume conservation is implicit, both three-dimensional velocity and vertical displacement are obtained directly from $\boldsymbol{\varphi}$, and the inversion of the horizontal potentials is easy (symbolically, $\boldsymbol{\varphi}_h = \nabla^{-2}\mathscr{A}_h$). The third prognostic equation is the explicit material conservation of the PV anomaly by contour advection on isopycnals ($\mathrm{d}\varpi/\mathrm{d}t = 0$), so that large PV gradients are not severely smoothed by diffusion. The disadvantage of this formulation is that the computation of the right-hand side of (2.3) and the inversion of the PV anomaly (2.4) are numerically costly.

REFERENCES

Bosart, L. F., Bracken, W. E. & Seimon, A. 1998 A study of cyclone mesoscale structure with emphasis on a large-amplitude inertia–gravity wave. *Mon. Wea. Rev.* **126**, 1497–1527.

Chow, K. C., Chan, K. L. & Lau, A. K. H. 2002 Generation of moving spiral bands in tropical cyclones. *J. Atmos. Sci.* **59**, 2930–2950.

Dritschel, D. G. & Viúdez, A. 2003 A balanced approach to modelling rotating stably-stratified geophysical flows. *J. Fluid Mech.* **488**, 123–150.

Farge, M. & Sadourny, R. 1989 Wave-vortex dynamics in rotating shallow water. *J. Fluid Mech.* **206**, 433–462.

Ford, R. 1994 Gravity wave radiation from vortex trains in rotating shallow water. *J. Fluid Mech.* **281**, 81–118.

Ford, R., McIntyre, M. E. & Norton, W. A. 2000 Balance and the slow quasimanifold: some explicit results. *J. Atmos. Sci.* **57**, 1236–1257.

Fritts, D. C. & Luo, Z. 1992 Gravity wave excitation by geostrophic adjustment of the jet stream. part i: Two-dimensional forcing. *J. Atmos. Sci.* **49**, 681–697.

Griffiths, M. & Reeder, M. J. 1996 Stratospheric inertia–gravity waves generated in a numerical model of frontogenesis: I: Model solutions. *Q. J. R. Met. Soc.* **122**, 1153–1174.

Lane, T. P., Doyle, J. D., Plougonven, R., Shapiro, M. A. & Sharman, R. D. 2004 Observations and numerical simulations of inertia–gravity waves and shearing instabilities in the vicinity of a jet stream. *J. Atmos. Sci.* **61**, 2692–2706.

Lane, T. P., Reeder, M. J. & Clark, T. L. 2001 Numerical modeling of gravity wave generation by deep tropical convection. *J. Atmos. Sci.* **58**, 1249–1274.

Lorenz, E. N. & Krishnamurthy, V. 1987 On the nonexistence of a slow manifold. *J. Atmos. Sci.* **44**, 2940–2950.

Luo, Z. & Fritts, D. C. 1993 Gravity wave excitation by geostrophic adjustment of the jet stream. part i: Three-dimensional forcing. *J. Atmos. Sci.* **50**, 104–115.

McWilliams, J. C. & Yavneh, I. 1998 Fluctuation growth and instability associated with a singularity of the balance equations. *Phys. Fluids* **10**, 2587–2596.

Miropol'sky, Yu. Z. 2001 *Dynamics of Internal Gravity Waves in the Ocean*. Kluwer.

Nappo, C. J. 2002 *An Introduction to Atmospheric Gravity Waves*. Academic.

O'Sullivan, D. & Dunkerton, T. J. 1995 Generation of inertia–gravity waves in a simulated life-cycle of baroclinic instability. *J. Atmos. Sci.* **52**, 3695–3716.

Pallàs-Sanz, E. & Viúdez, A. 2007 Three-dimensional ageostrophic motion in mesoscale vortex dipoles. *J. Phys. Oceanogr.* **37**, 84–105.

Pfister, L., Chan, K. R., Bui, T. P, Bowen, S., Legg, M., Gary, B., Kelly, K., Proffitt, M. & Starr, W. 1993 Gravity-waves generated by a tropical cyclone during the step tropical program - a case-study. *J. Geophys. Res.* **95**, 8611–8638.

Plougonven, R., Teitelbaum, H. & Zeitlin, V. 2003 Inertia gravity wave generation by the tropospheric midlatitude jet as given by the fronts and atlantic storm-track experiment. *J. Geophys. Res.* **108**, doi:10.1029/2003JD003535.

Reeder, M. J. & Griffiths, M. 1996 Stratospheric inertia–gravity waves generated in a numerical model of frontogenesis: Ii: Wave sources, generation mechanisms and momentum fluxes. *Q. J. R. Met. Soc.* **122**, 1175–1195.

Saujani, S. & Shepherd, T. G. 2002 Comments on "balance and the slow quasimanifold: some explicit results". *J. Atmos. Sci.* **59**, 2874–2877. Reply: *J. Atmos. Sci.* **59**, 2878–2882.

Snyder, C., Muraki, D. J., Plougonven, R. & Zhang, F. 2007 Inertia–gravity waves generated within a dipole vortex. *J. Atmos. Sci.* (in press).

Snyder, C., Skamarock, W. C. & Rotunno, R. 1993 Frontal dynamics near and following frontal collapse. *J. Atmos. Sci.* **50**, 3194–3211.

Vanneste, J. & Yavneh, I. 2004 Exponentially small inertia–gravity waves and the breakdown of quasigeostrophic balance. *J. Atmos. Sci.* **61**, 211–223.

Viúdez, A. 2006 Spiral patterns of inertia–gravity waves in geophysical flows. *J. Fluid Mech.* **562**, 73–82.

Viúdez, A. 2007 The stationary frontal wave packet spontaneously generated in mesoscale dipoles. *J. Phys. Oceanogr.* (in press).

Viúdez, A. & Dritschel, D. G. 2003 Vertical velocity in mesoscale geophysical flows. *J. Fluid Mech.* **483**, 199–223.

Viúdez, A. & Dritschel, D. G. 2004 Optimal potential vorticity balance of geophysical flows. *J. Fluid Mech.* **521**, 343–352.

Viúdez, A., Tintoré, J. & Haney, R. L. 1996 About the nature of the generalized omega equation. *J. Atmos. Sci.* **53**, 787–795.

Williams, P. D., Haine, T. W. N. & Read, P. L. 2005 On the generation mechanisms of short-scale unbalanced modes in rotating two-layer flows with vertical shear. *J. Fluid Mech.* **528**, 1–22.

Williams, P. D., Read, P. L. & Haine, T. W. N. 2003 Spontaneous generation and impact of inertia–gravity waves in a stratified two-layer shear flow. *Geophys. Res. Lett.* **30**, doi:10.1029/2003GL018498.

Yavneh, I. & McWilliams, J. C. 1994 Breackdown of the slow manifold in the shallow-water equations. *Geophys. Astrophys. Fluid Dyn.* **75**, 131–161.

Yuan, L. & Hamilton, K. 1994 Equilibrium dynamics in a forced-dissipative f-plane shallow-water system. *J. Fluid Mech.* **280**, 369–394.

Zhang, F. 2004 Generation of mesoscale gravity waves in upper-tropospheric jet-front systems. *J. Atmos. Sci.* **61**, 440–457.